REVIEW OF AERONAUTICAL FATIGUE INVESTIGATIONS IN POLAND (2015 – 2016)

by

Dr Antoni Niepokólczycki
Institute of Aviation, Warsaw, POLAND
(Investigations in Civil Aviation)

and

Dr Krzysztof Dragan
Air Force Institute of Technology, Warsaw, POLAND
(Investigations in Military Aviation)

35 Conference of the International Committee on Aeronautical Fatigue and Structural Integrity, Nagoya, Japan, June 5-6, 2017

INVESTIGATIONS IN CIVIL AVIATION

1. EVALUATION OF DAMAGE DEGREE OF INCONEL 718 USING NONDESTRUCTIVE INDICATORS OF DAMAGE

Introduction

In engineering materials and structures, damage to the material can be defined as a decrease in resistance to destruction. Fatigue damage of the material is caused by cyclic loading and increases with the number of cycles in a cumulative way, which in effect may lead to the destruction of the object.

The difficulty of measuring the degree of damage of the material under load is related to a lack of well-defined measure of damage, the local character of the damage process, and different mechanisms of damage associated with the generation and types of loads and operating conditions. Depending on the character of damage in the material, or on the definition of destruction, the effectiveness of damage parameters can vary. Selection of an appropriate damage parameter is of key importance to modeling failure or life prediction. The measure of damages does not have a universal character. They are selected depending on the stage of development of defects, and may involve different mechanisms of defects' generation, and different stages of process failure and destruction.

Methods of measuring material damage are based on the assumption that there is a correlation between the degree of damage and the measurable physical quantity called damage indicator. Usually, the damage indicator is directly chosen out of a number of the mechanical quantities of interest, while the measuring parameters are selected from either mechanical or physical quantities. In order to determine the degradation of the material, both destructive and nondestructive methods are used. An important advantage of nondestructive methods is that they do not require taking a sample of the material from the tested object to determine its material properties. In this work, the ultrasonic and eddy current method were selected to detect changes in the structure of the material. In ultrasonic testing, attenuation of ultrasonic waves and acoustic birefringence were used as indicators of damage. In the case of the eddy current method, change in the phase angle of impedance in the material was selected as a damage indicator.

The test material and specimens

Inconel 718 was the material used to test and evaluate the degradation. Inconel is a family of alloys of austenitic crystal structure based on nickel and chromium. These superalloys are characterized by high heat resistance, strength and creep resistance at high temperatures, surface stability and resistance to corrosion and oxidation. Therefore, Inconel alloys are typically applied in extreme working conditions including in the power engineering industry, aviation and aerospace.

In order to obtain a certain degree of deformation of the material samples, static tensile tests and creep tests were carried out. To investigate the material's degradation, a new type of specimen with variable cross-sectional area of the measuring part (Fig. 1.) was used. This allowed researchers to obtain a continuous distribution of plastic strain in that part of the specimen. The deformation that varies along the axis of the sample enables analysis of

damage induced by plastic deformation. The proposed method enables replacing a series of specimens with a single sample. The test method and specimen are protected by patent.

Fig. 1. Specimen used to test degradation of Inconel 718

Evaluation of a damage degree of Inconel 718

After the tests, the measurements of permanent deformations in the directions of width and thickness of the specimen were performed. Then, from the condition of incompressibility of the material, the deformation values were calculated in the direction of the sample's axis. Based on the calculated deformation values, the values of a damage parameter D were calculated using the model of Johnson:

$$D = \sum \frac{\Delta\varepsilon}{\varepsilon^f} \quad (1),$$

where: $\Delta\varepsilon$ is the permanent deformation in the direction of the axis of the sample,
ε^f is the final parameter value corresponding to the breaking of the sample.

Fig. 2. shows the distribution of the damage parameter calculated as the function of the distance from the fracture after the test (the distance from the smallest cross-section). The value of $\Delta\varepsilon$ in the marked places $\Delta\varepsilon_i$ was calculated from the relation:

$$\Delta\varepsilon_i = -\left(\frac{a_i - a_0}{a_0} - \frac{b_i - b_0}{b_0}\right) \quad (2),$$

where: a_0 is the width of the specimen in the marked place i before strength tests,
a_i is the width of the specimen in the marked place i after strength tests,
b_0 is the thickness of the specimen in the marked place i before strength tests,
b_i is the thickness of the specimen in the marked place i after strength tests.

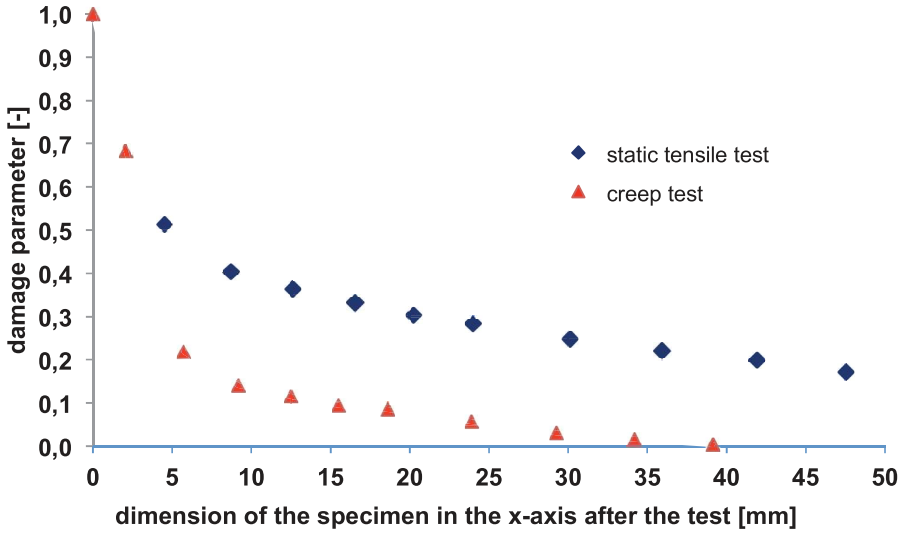

Fig. 2. Damage parameter as the function of the distance from the fracture for a specimen after static tensile test and after creep test

Evaluation of a damage degree in Inconel 718 using the attenuation coefficient of ultrasonic waves

The amplitude of the ultrasonic wave propagating in the material decreases with increasing distance. This phenomenon is associated with acoustic attenuation - loss of acoustic energy that occurs between any two points of travel. This loss is mainly due to scattering and absorption mechanisms and to geometric factors. Scattering in metallic materials is caused by very small discontinuities, such as precipitation, and also by larger areas such as grain boundaries. Dislocation along with magnetic and thermoelastic damping are major types of absorption mechanisms. Geometric factors include diffraction, beam spreading and coupling losses.

The measurement of ultrasonic attenuation (dB) or of the attenuation coefficient (dB/mm) allows nondestructive determination of certain material conditions and properties. Attenuation measurements may be a factor when the material is highly attenuative and the critical flaw size rather small. Attenuation mesurements are usually used to verify material uniformity and to assess material properties.

Prior to creep tests and the static tensile tests, the attenuation coefficient of ultrasonic waves was measured. The average values of the attenuation coefficient in the measuring part of individual specimens fell in the range of 0.12-0.13 dB/m - the biggest difference between the mean values of the coefficient did not exceed 0.01 dB/mm. The differences of the attenuation coefficient measured along the x axis for individual samples did not exceed 0.04 dB/mm. Fig. 3. shows the values of the attenuation coefficient in the measuring part of the specimens before strength tests.

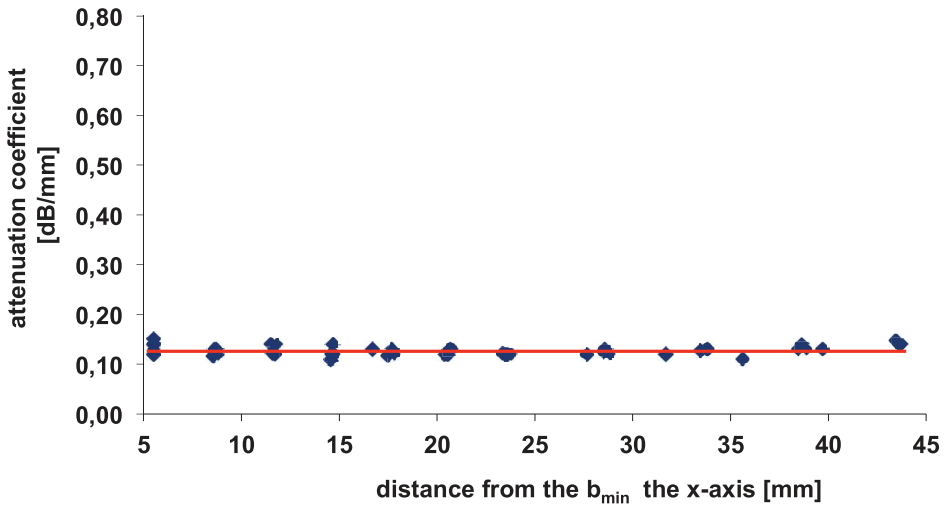

Fig. 3. The values of the attenuation coefficient in the measuring part of the specimens before testing

The attenuation coefficient of the material, after degradation caused by creep or tensile tests, was differ than before testing. After creep testing, there was approximately a twofold increase in the value of the attenuation coefficient in the measurement part of the specimens. The damage parameter values in this area fell in the range of 0 - approx. 0.13 (Fig. 4.). However, the increase in the coefficient values in this area, despite some monotonicity, was characterized by local fluctuations. There was a large increase in the coefficient only for the damage parameter values of approx. 0.18, so in the measured area near the fracture.

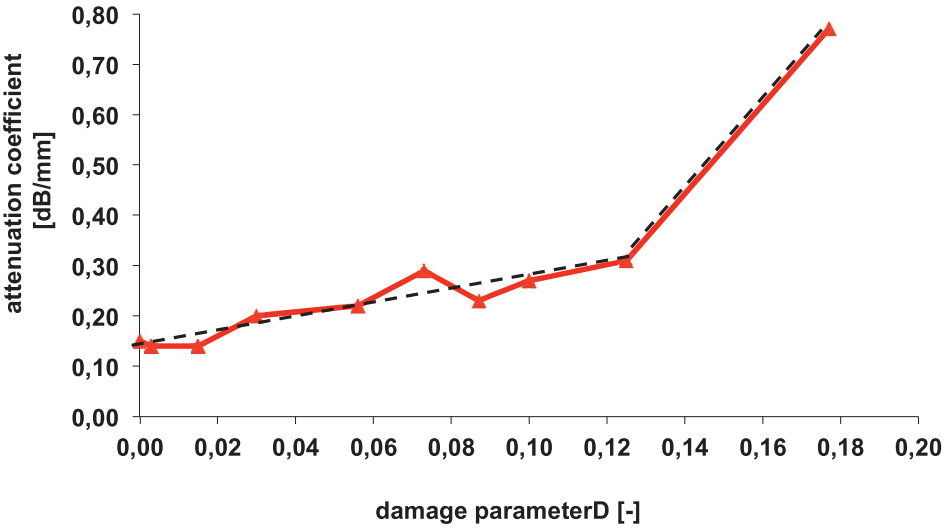

Fig. 4. The values of the attenuation coefficient in the measuring part of the specimens after creep tests

After static tensile tests, changes in the value of the attenuation coefficient depending on the damage parameter can be divided into a few stages (Fig. 5.). In the measuring part for

damage parameter lesser than D ~ 0.25, the value of the attenuation factor, despite some variations, remained at a constant level, higher than those for the samples prior to destructive testing by about approx. 30%. While at the second stage, with the degradation of the material above D ~ 0.25 an approximately linear increase in the value of the attenuation was observed. For values of D ~ 0.37 this increase amounted to approx. 75%. Next, in the third measurement area for the damage parameter D = 0.41, the value of attenuation coefficient was around four times higher than for the specimens before the static tensile tests.

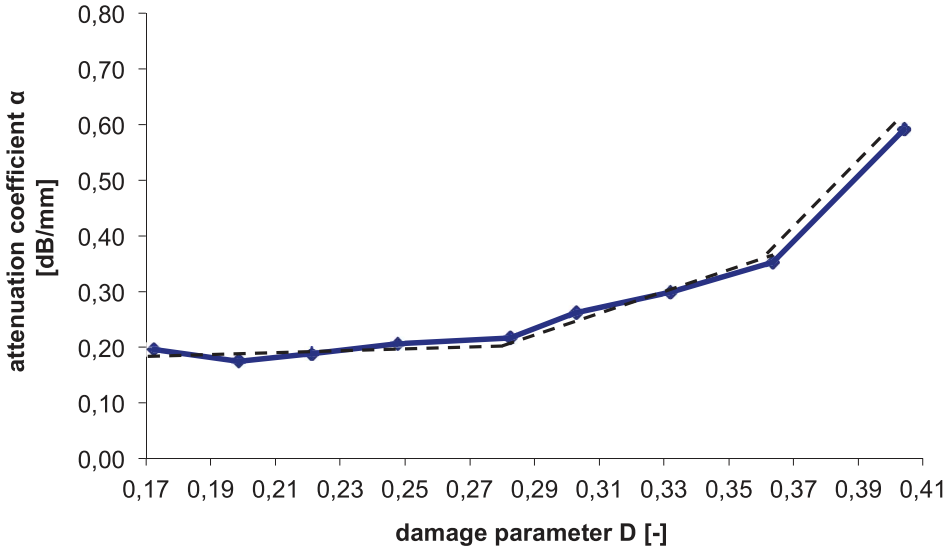

Fig. 5. The values of the attenuation coefficient in the measuring part of the specimens after static tensile tests

Evaluation of a damage degree of Inconel 718 using acoustic birefringence

The anisotropy of the elastic properties are manifested by different velocities of the propagation of ultrasonic waves in the material. These speeds are dependent on the direction of wave propagation in the material or on their polarity. This type of anisotropy is known as acoustic birefringence. Acoustic anisotropy of the material may be characterized by the values of the algebraic combinations of different types of wave velocity in different directions of propagation and of different polarities.
The speed of transverse waves propagating in the thickness direction was measured at two mutually perpendicular positions of the ultrasonic probe, i.e. mutually perpendicular polarization of waves. In the tests, an ultrasonic probe with a frequency of 4MHz was used.
The coefficient of birefringence, is defined by the following relation:

$$B = \frac{V_{T2} - V_{T1}}{0{,}5(V_{T2} + V_{T1})} \qquad (3),$$

where: VT1, VT2 - velocity of transverse waves propagating in the direction of the specimen thickness and polarized in mutually perpendicular directions.

The measurements of acoustic birefringence were carried out before strength tests - static tensile tests and creep tests. The average value of birefringence in the measuring part was - 0.0151, and the difference value of birefringence for the individual areas was lesser than 0.0013. Fig. 6. shows the values of birefringence in the measuring part of specimens before strength tests.

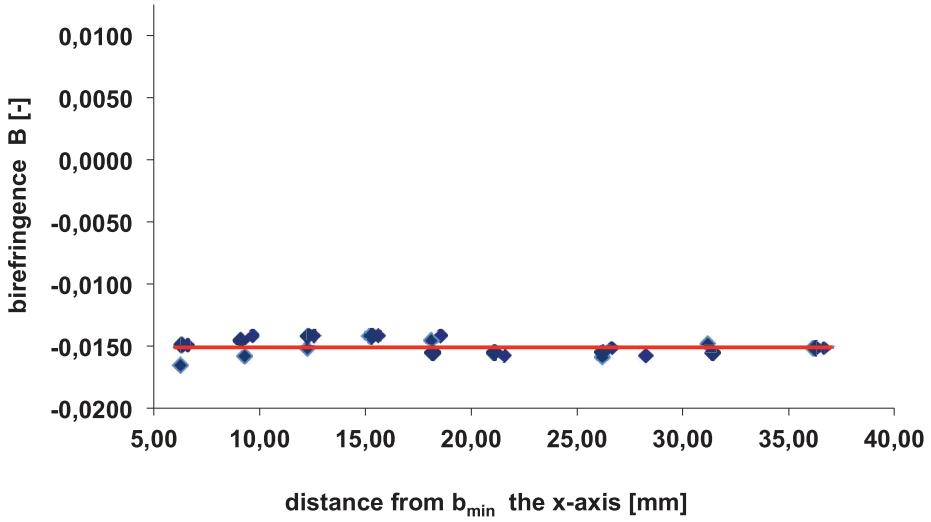

Fig. 6. The values of birefringence in the measuring part of the specimens before testing

The values of acoustic birefringence after static tensile tests fell in the range from - 0.0127 to 0.0026 for the measuring areas with the greatest degree of damage. Across the whole of the measuring part the change in birefringence totaled 0.0153. The results of tests for the measuring part are shown in Figure 7.

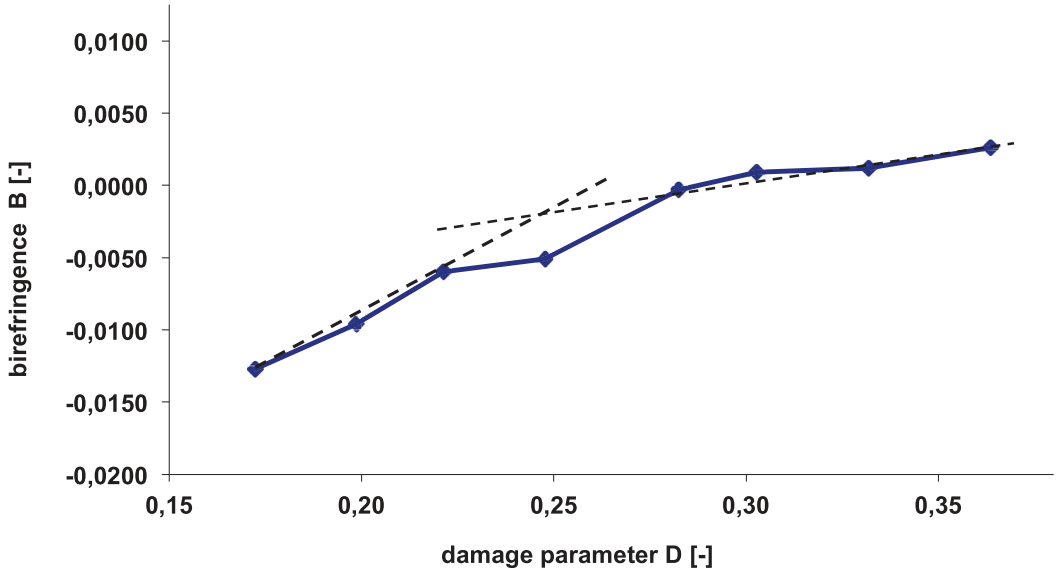

Fig. 7. Changes of birefringence after static tensile tests in the measuring part depending on the damage parameter

For the specimens after a creep tests, changes of acoustic birefringence fell in the range from -0.0148 to -0.0122. The value of birefringence was the lowest in the gripping part. In the measuring part there was a slight increase reaching the maximum in the highest value of the parameter of damage. In the measuring part the increase in birefringence totaled 0.0029. Fig. 8. shows the change of birefringence B as a function of damage parameter D in the measuring part of the specimen.

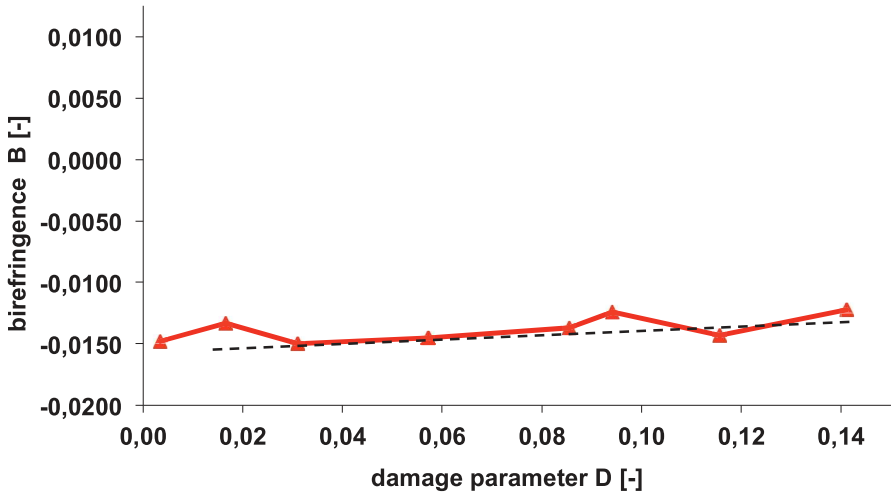

Fig. 8. Changes of birefringence after creep tests in the measuring part depending on the parameter of damage

Evaluation of a damage degree of Inconel 718 using the eddy current phase angle

The eddy current method is used for materials which show electrical conductivity. It can be performed both on ferromagnetic and non-ferromagnetic materials. The method makes possible to detect surface and subsurface discontinuities such as cracks and corrosion and can be also used to measure coating thickness and to compare the structure of materials. The eddy current method can be used to detect discrete defects in metallic materials and to assess selected conditions and material properties. It is also becoming more widely used for research and evaluation of changes in the physical properties of materials. The degradation of the material microstructure associated with the development of local plastic deformation leads to changes in the phase angle of complex impedance of the eddy current in the material. The phase angle value of eddy currents in the material depends mainly on the electrical conductivity and magnetic permeability of the material. Subtle changes in these parameters due to either the change in stress or a local change in the composition or density of the material affect a change of the phase angle. Measuring the phase angle shift allows not only to assess the stress changes, but it also yields information about changes in the properties and/or the microstructure resulting from the degradation processes.

Measurements of the angle phase in specimens before strength test was performed for evaluating the homogeneity of the measured parameter over the entire surface of the sample. Tests were performed at the frequency of the electromagnetic coils between 50 - 150 kHz, allowing to obtain depth of the eddy currents penetration into the test material, suitably 2.53 mm and 1.46 mm. The frequency was chosen so that the depth of penetration did not exceed the thickness of the specimen in the smallest cross section. The phase angles on the specimens before, and next, after strength tests were measured.

For the specimens before strength tests, the value of the phase angle was approximately constant. The differences in the measuring parts of specimens fell within the range of 1.3 ° (Fig. 9.).

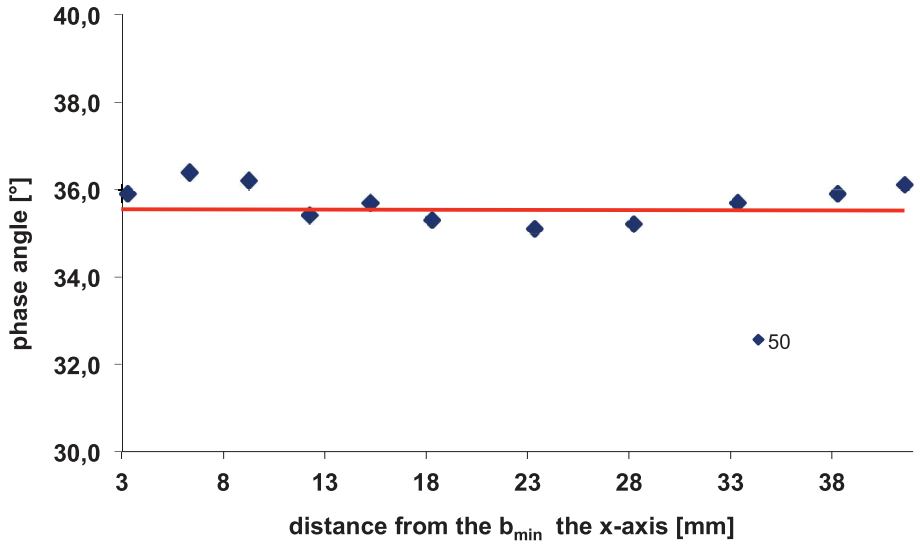

Fig. 9. The values of the phase angle in the measuring part of the specimens before testing

In the case of specimens after creep testing, the changes in the phase angle had a similar distribution to that of the specimens prior to creep testing (Fig. 10). But the obtained degree of deformation in the measurement part was limited to the value of the damage parameter D = 0.22 at a distance of 5.71 mm from the fracture.

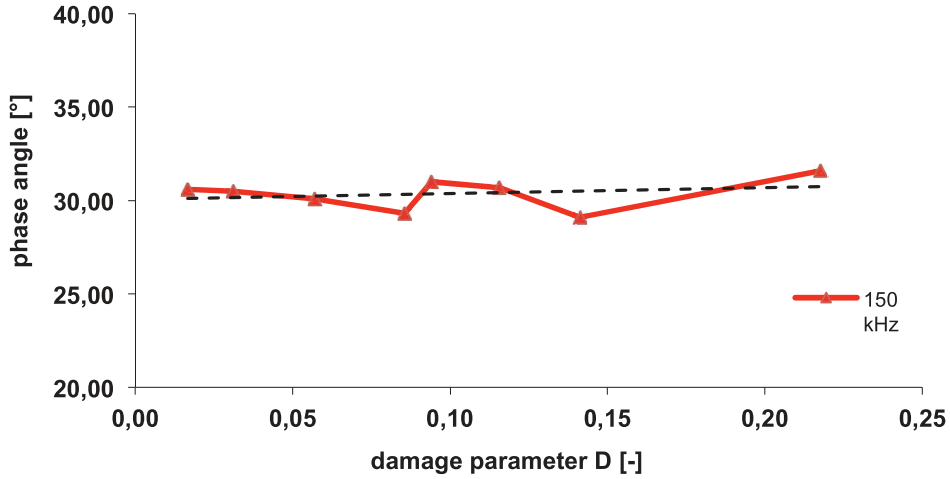

Fig. 10. The values of the phase angle in the measuring part after creep tests

Fig. 11. shows changes in the angle phase impedance depending on the value of the damage parameter of the material after static tensile tests. For the measurement purposes, the eddy current transducers with frequencies of 50 kHz and 150 kHz were used. For both frequencies, it was found that the value of the phase angle decreased while the damage parameter increased. For the entire sample, a decline in the value of the phase angle was approx.. 25° and 10° for the frequencies of 150 kHz and 50 kHz, respectively. In both cases,

there are two stages of the changes in the phase angle. In areas of damage parameter below D ~ 0.25 there are smaller changes of the angle phase and smaller stability of the direction of change. Above D ~ 0.25 decrease in the value of the phase angle is dynamic and almost linear (large changes of value, greater stability of direction changes). The described stages of the changes in the phase angle indicated by broken lines in Fig. 11.

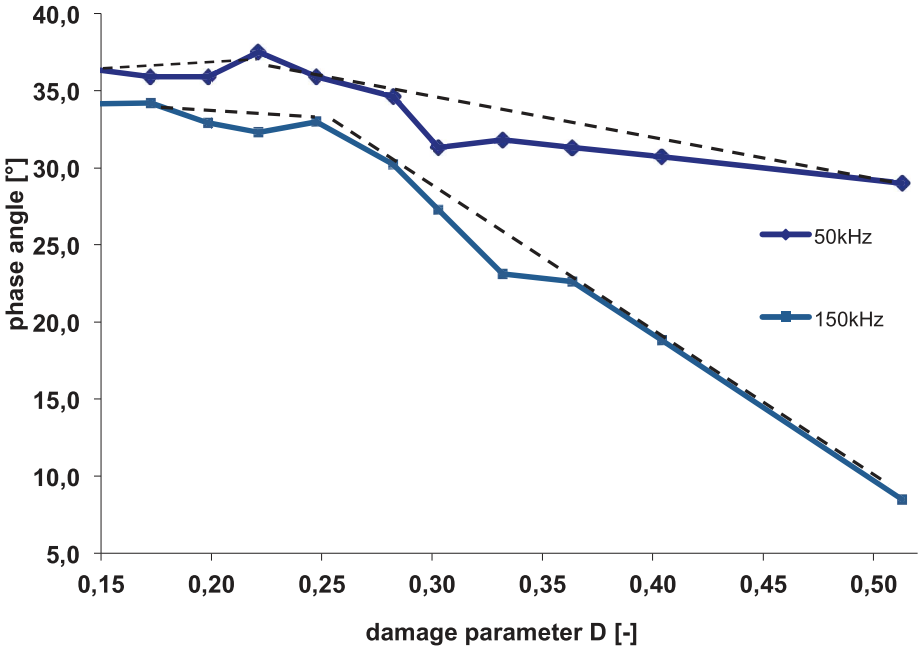

Fig. 11. The values of phase angle in the measuring part of the specimens after static tensile tests

Summary and conclusions

Inconel 718 was the material used to test and evaluate the degree of the material's degradation. For the tests, specimens with a variable cross-sectional area of the measuring part were used. In order to obtain a certain deformation of the material, static tensile tests and creep tests were carried out. To evaluate the degree of damage to the material, the nondestructive indicators were used. With an increasing degree of material deformation, changes in the values of the nondestructive indicators were received. The changes in damage indicators after the tensile tests were definitely higher than those after creep tests. Also, the deformations of the material estimated by the parameter of damage were lesser for the specimens after creep testing than after static tensile testing.

In the case of the attenuation coefficient, for deformation caused by creep and static tensile tests, the damage indicators increased significantly in the areas close to the fracture.

A acoustic birefringence of the material subjected to creep tests increased slightly. The maximum increase in the value of the birefringence was approx. 20% compared to the state before the test. Changes in the value of birefringence for the specimens after creep tests had the character of local increases and decreases. Upon subjecting the material to static tensile testing the values of acoustic birefringence increased approx. 100% compared to the state before the tests. The increases in birefringence were approximately proportional to the increase in the damage parameter.

The measurements results of the phase angle of eddy currents showed a nearly linear decrease in their values with an increase in the damage parameter of the material. This only applies to the material after static tensile tests. In the case of specimens after creep tests (small value of damage parameter) there was no change of the phase angle - there were only local fluctuations recorded.

To summarize, all three indicators showed changes in damage degree of the material subjected to degradation. The increase in the attenuation coefficient was observed following strength tests in all areas of the samples. However, its significant growth occurred at in the final stage of the process of destruction. The high dynamics of changes in the phase angle was found at about the damage parameter above $D = 0.25$, while acoustic birefringence changed significantly at earlier stages of destruction.

2. ELECTROPOLISHING PROCEDURE DEDICATED TO IN-DEPTH STRESS MEASUREMENTS WITH X-RAY DIFFRACTOMETRY

Introduction

Electropolishing: its advantages and disadvantages

In the electrolytic polishing procedure, which nowadays is very well recognized, the disposal of the outer layer of the material is performed by removing it ion by ion. Electropolishing was invented in 1929 by Pierre Jacquet and was used for the first time in 1935 in preparing metallographic sample. This technique can be used instead of many different types of surface treatment including milling, grinding, blasting and buffing. Electropolishing involves submerging the object into the electrolyte dedicated to the type of the material. Simultaneously, the object is subjected to an electrical current. During the electropolishing process, the object is maintained anodic. The phenomena accompanying electropolishing are the saturation of the surface with the dissolved metal and the rise of the temperature resulting the gassing effect.

The main advantage of electropolishing is the quality of the smooth surface created on the metal object is higher than if obtained by any method involving mechanical polishing. Additionally, from the in-depth stress measurement point of view (for example with X-ray diffraction methods) electropolishing neither disturbs the stress distribution nor introduces any additional values of stresses. The result of electropolishing is a surface without any defined microscopically features i.e. with neither torns nor pits: the surface becomes microscopically smooth, bright and clean. Electropolishing removes scratches and deformations due to cutting or grinding. Another advantage of electropolishing is the reduction of the friction coefficient value. Compared to the mechanically finished surface, the friction coefficient can be even 75% lower. Unfortunately, alongside the above advantages there are also drawbacks. The main disadvantage is associated with polishing multiphase alloys and composites due to different polishing rates of the ingredients.

The main difference between electropolishing and mechanical polishing is that the later always leaves smears, scratches, strains, metal debris and abrasives embedded in the surface of the object. Electropolishing unveils the crystal structure while finishing processes which abrasives employ always somehow deform and tamper with the metal surface: abrasives penetrates into the metal becoming inserted in the surface. The influence of the mechanical treatment can be very significant from the material strength point of view; for example the finishing operations of steel can lead to a threefold decrease in tensile strength.

The electropolishing procedure is not always easy to perform. Sometimes it is necessary to perform the initial treatment with abrasives before appropriate electrolytic polishing, especially when e.g. orange peel or mold surface texture are visible.

Although there is no universal, applicable procedure for electropolishing there are some indications for the sample preparation prior to electropolishing and some suggestions on parameters affecting electropolishing. Before electropolishing, the sample should be finished by mechanical polishing (600-grit). During electropolishing, the correct combination of bath temperature, voltage, current density, and time should be applied: the metallographer has to control many experimental variables.

Theoretical background

The first step in working out the electropolishing procedure for the material-electrolite sets is to prepare the curve for the relation: applied voltage versus current density. A typical curve of current density versus voltage is shown in Fig. 1. It helps to establish the most appropriate current and voltage parameters in order to obtain best polishing results. Three stages can be observed. At the first stage, for low voltage values where the almost linear dependence (A-B) appears, etching occurs. The second stage (C-D) is the most interesting for the electropolisher as this is when electropolishing takes place. The last stage (D-E) for high voltages is the region of gas evolution and pitting. The optimal parameters for electropolishing are defined by point C.

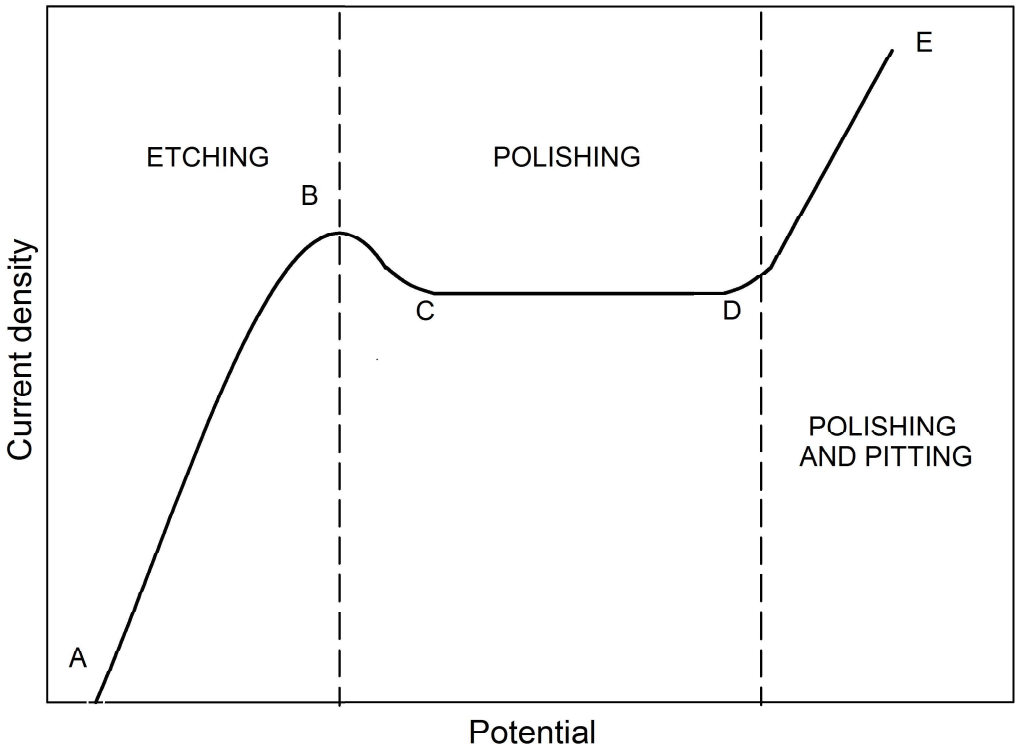

Fig. 1 The typical relation between current density versus voltage for electropolishing

To delineate the current vs. voltage plot the cathode area should be much larger than the anode surface area. In this condition, liberation of hydrogen does not affect the shape of the curve. It is important remember that the shape of the curve depends on the processes occurring at the anode.

Unfortunately, it was impossible to work out one universal theory of the electropolishing procedure due to too many independent variables affecting the process. Nevertheless, the solutions to typically occurring problems were developed and presented in ASTM Standard E3 [3], see table 1.

Table 1. Problems possible to occur during the electropolishing and its corrections

Trouble	*Possible cause*	*Suggested solution*
Center of the specimen deeply etched	No polishing film at the center of the specimen	– Increase voltage – Decrease agitation – Use more viscous electrolyte
Pitting or etching at edges of specimen	Too viscous or thick film	– Decrease voltage – Increase agitation – Use less viscous electrolyte
Sludge settling on the surface	Insoluble anode product	– Try new electrolyte – Increase temperature – Increase voltage
Roughness or matte surface	Insufficient or no polishing film	– Increase voltage – Use more viscous electrolyte
Waviness or streaks on the polished surface	Insufficient time Incorrect agitation Inadequate preparation Too long time	– Increase or decrease agitation – Use better preparation – Increase voltage or decrease time
Stains on polished surface	Attack after polishing current is off	– Remove specimen while current is still on – Try less corrosive electrolyte
Unpolished spots (bullseyes)	Gas bubbles	– Increase agitation – Decrease voltage
Phases in relief	Insufficient polishing film	– Increase voltage – Use better preparation – Decrease time
Pitting	Polishing too long Voltage too high	– Use better preparation – Decrease voltage – Decrease time – Try different electrolyte

The most important factor from the electropolishing procedure point of view is the rise of temperature, which causes the subsequent phenomena: a decrease in the electrolyte resistance, the plateau current density decrease, the bath viscosity decrease (making it more difficult to maintain a viscous anode layer) and, in consequence, the deterioration of the surface quality. Naturally, both the type of the electropolished material and the type of the electrolyte affect the time needed to remove a layer of a desired thickness: generally the higher the plateau current density, the shorter time is needed. It is worth to notice that long electropolishing times can result in some undesirable artifacts such as surface waviness and relief accentuation.

Experiment

Material and specimens

The materials chosen for the experiment were: stainless steel 1H13 and aluminium alloy 2024.

1H13 stainless steel is a semi-ferritic steel used in valves, hydraulic presses, steam turbine blades and nuts production. Its chemical composition and some physical properties are presented in tables 2 and 3.

Table 2. Different standards designations for 1H13 martensitic stainless steel and its chemical composition

Other standards designations		Chemical composition [%]	
EN	1.4006	C	0,08 – 0,15
DIN	X12Cr13	Cr	11,50 – 13,50
AISI	410	Si	≤ 1,00
Russia	12Ch13	Mn	≤ 1,50
Others	2302 1Cr12	Ni	≤ 0,75
		S	≤ 0,015
		P	≤ 0,040

Table 3. Mechanical and physical properties of 1H13 stainless steel

Mechanical properties		Physical properties	
R_m	$700 - 850MPa$	density at $20°C$	$7{,}7\ kg/dm^3$
R_e	$450 - 500MPa$	E	$215GPa$
percentage elongation after fracture	20%	thermal expansion coefficients	$20℃ - 200℃: 11 \cdot 10^{-6}K^{-1}$
hardness			$200℃ - 400℃: 12 \cdot 10^{-6}K^{-1}$
hardened and tempered	$\geq 24HRC$	coefficient in thermal conductivity	$30W/(mK)$
softened state	$220HB$	specific heat at 20℃	$460\ J/(kg \cdot K)$
		resistivity	$0{,}6\ (\Omega \cdot mm^2)/m$

The second investigated material was 2024-T3 aluminium alloy, which is characterized by good machinability and surface finish capabilities. This alloy is used in aircraft fittings, gears and shafts, bolts, clock parts, computer parts, couplings, fuse parts, hydraulic valve bodies, missile parts, munitions, nuts, pistons, rectifier parts, worm gears, fastening devices, veterinary and orthopedic equipment and structures.

Table 4. Different standards designations for aluminium alloy 2024T3 and its chemical composition

Other standards designations		Chemical composition [%]	
EN AST M	2024	Si	$\leq 0{,}5$
DIN	AlCu4Mg 1 AlCu4Mg 2	Fe	$\leq 0{,}5$
Russi a	1160 D16	Cu	$3{,}8 - 4{,}9$
		Mn	$0{,}3 - 0{,}9$
		Mg	$1{,}2 - 1{,}8$
		Cr	$\leq 0{,}1$
		Zn	$\leq 0{,}25$
		Ti	$\leq 0{,}15$
		Zr	$\leq 0{,}1$

Table 5. Mechanical and physical properties of 2024T3 aluminum alloy

Mechanical properties		Physical properties	
R_m	$360 - 435MPa$	density in $20°C$	$2{,}78\, kg/dm^3$
R_e	$250 - 290MPa$	E	$730GPa$
percentage elongation after fracture	$12\% - 14\%$	thermal expansion coefficients	$23{,}1\ \mu m/mK$
hardness	$104 - 123$	coefficient in thermal conductivity	$121\ W/(mK)$
		specific heat at 20℃	$874\ J/(kg \cdot K)$

1H13 stainless steel was mechanically polished and 2024T3 aluminium alloy specimen was a sheet of metal as delivered.

The equipment and electrolyte used during the experiment

The equipment used for the experiment was the mobile polisher and etcher dedicated to the local outer layer removal, KR650 by ATM Company (Fig. 2). It allowed operators' to perform electropolishing only in the chosen area in where the stress state was known.

Fig. 2. KR650 mobile electropolisher

Electropolishing is performed by the head with a long house providing the electrolyte and being the cathode. Polishing and etching gets automatically ready by touching the piezo button at the handle. The equipment enables electropolishing even on an area of 9mm in diameter and on complex surfaces with curvature. The flow of electrolyte voltage, current intensity and time can be regulated. The power available is 160W and the range of voltage is 90V DC while the maximum current value is 2A.

The electrolyte used during the experiment was the K1 electrolyte dedicated to all steel types, alluminium and its alloys, nickel, tin, and titanium. K1 electrolyte is a mixture of perchloric acid, ethanol and Propandiol-1,2.

Plateau region determination

Prior to conducting the main part of the experiment (determining the relationship between time of electropolishing and the thickness of electropolished layer), the electropolishing parameters had to be determined. In order to do so, electropolishing was performed for both materials. The voltage value was a variable during the experiment and the current intensity was the measured value. The results are presented in Figs. 3 and 4.

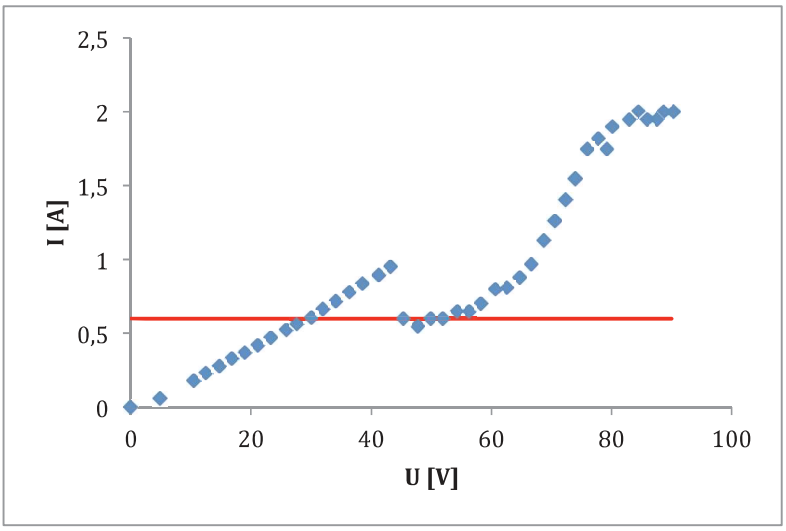

Fig. 3. The I-U characteristic during electropolishing for stainless steel 1H13

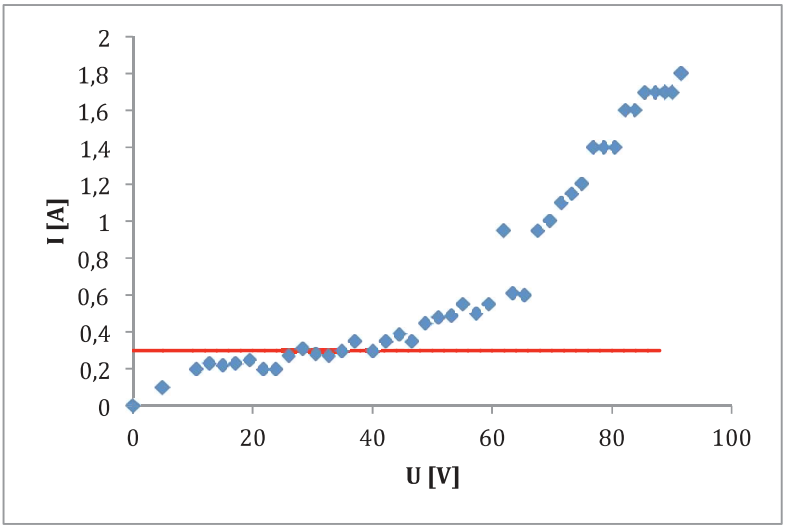

Fig. 4. The I-U characteristic during electropolishing for 2024T3 aluminium alloy

The plateau region of the above plots was selected as $0{,}6A$ for the chosen type of steel and $0{,}3A$ for aluminium alloy 2024T3. For these current values, the electropolishing process should be performed in an optimal way.

Electropolished depth vs. time relationships

The relationship between the thickness of the electropolished layer and the duration of the process is crucial for in depth stress measurements. The linear relatonship between these values was assumed. The measurement was performed once for both materials in the time range of $300s$. For stainless steel, the optimal current value was set i.e. $0{,}6A$ and the time interval was $30s$ in the time range $0 - 120s$, while above $120s$ the time interval was $15s$. For aluminium alloy the optimal current value was twice lower (i.e. 0,3A) and the time interval was 10s for values 0 – 240s, the additional electropolishing was performed for the time of 300s.

Selected electropolished surfaces are presented in Fig. 5.

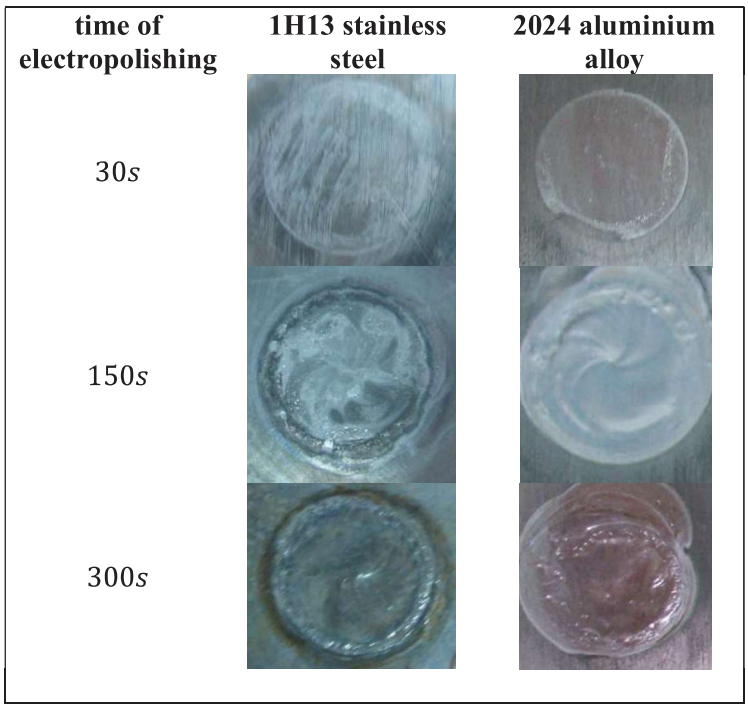

Fig. 5. Surface after electropolishing

The electropolished layer thickness measurements were performed with a depth sensor whose accuracy was 0,01mm. The results are presented in Figs. 6 and 7.

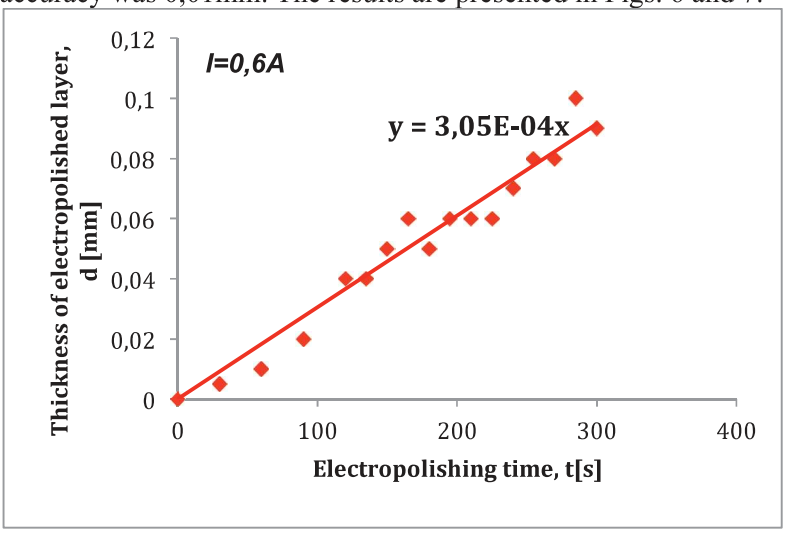

Fig. 6. Electropolished layer thickness versus electropolishing time for stainless steel 1H13. Current for electropolishing process was I=0,6A

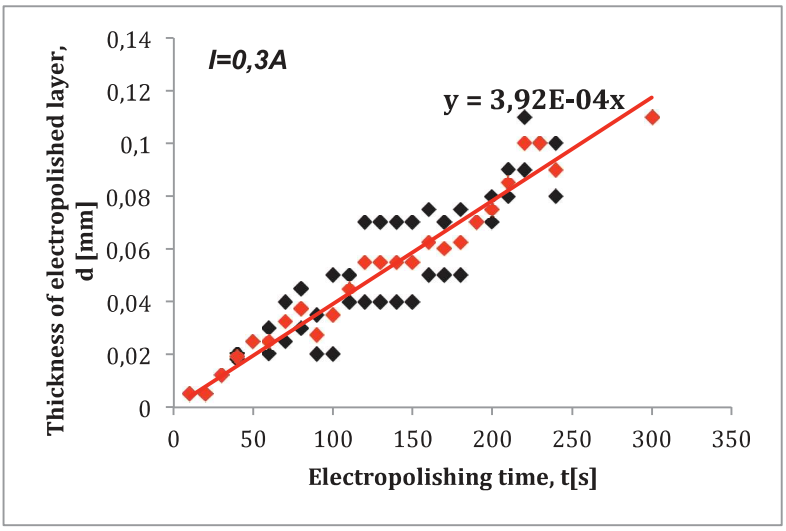

Fig. 7. Electropolished layer thickness versus electropolishing time for aluminium alloy 2024T3. Current for electropolishing process was I=0,6A

The measurement points were approximated by linear dependency: the slope for the steel was $3{,}05 \cdot 10^{-4}$ and for aluminum alloy: $3{,}92 \cdot 10^{-4}$. The plots allow determining the time values necessary to electropolish the needed layer. Additionally it allows predicting the time values for deeper electropolishing by extrapolating the obtained plot. To remove a layer of $0{,}01m$ of 1H13 steel, the electropolishing procedure should last about $33s$, while for 2024T3 aluminium alloy it is $25s$.

Conclusions

Voltage-current characteristics for the electropolishing process were obtained for two materials: 1H13 stainless steel and 2024T3 aluminium alloy. This allowed researchers to choose the optimal parameters for the electropolishing procedure. The relation between depth and duration of electropolishing was determined. This would allow the removal of a very precisely defined layer for e.g in-depth diffraction stress measurements. It was also concluded that with a thick layer (e.g. 0,1mm) it is better to perform electropolishing incrementally rather than for a long time at one go (300s). As Fig. 5 shows, the surface of the area electropolished for a relatively shorter time is smoother than those surfaces electropolished longer. Moreover, incremental electropolishing allows a better controll of the specimen and electrolyte's temperature.

3. LIGHTNING STRIKE PROTECTION OF AIRCRAFT COMPOSITE STRUCTURES: ANALYSIS AND COMPARATIVE STUDY

Introduction

Changes occurring over the last decades in design philosophy of many aircraft structures, in particular the application of fibre-reinforced composites with a polymeric matrix in the exterior fuselage, allowed the strength-to-mass ratio to be significantly increased, which resulted in the possibility of achieving higher speeds and manoeuvrability while keeping fuel consumption at a lower level. However, the usage of polymeric composites in manufacturing aircraft structures resulted in one drawback with respect to the lightning phenomena. Since polymers applied are dielectrics, the lightning strike events occurring during aircraft operation cause serious damage to such structures. This, in turn, requires expensive repairing and testing, and obviously, grounding the aircraft for the period of up to 6 working days, leading to increased operational costs.

A lightning striking a structure made of polymeric composite initiates numerous accompanying phenomena, which additionally intensify structural degradation and disintegration. Lightning strikes usually occur during take-off and landing of an aircraft as well as during passing through the storm clouds. Lightning usually strikes a geometrically extremal point of an aircraft (like radome, wing tips, etc.) and travels through the structure along the shortest path, which is additionally the most conductive one, to exit at another geometrically extremal point. During this process several accompanying phenomena occur. A high electrical discharge causes that almost insulating air becomes plasma with a very good conducting ability, and in the resulting lightning channel the temperature rapidly rises (locally even up to 30000 K). The most influencing phenomena accompanied such an event are overpressure and resistive heating. The first one results from the appearance of an acoustic wave (when air fills the empty lightning channel) which interacts mechanically with a stroked structure and causes the external layers of the composite structure to break down and a net of cracks and delaminations to appear in the vicinity of the stroked area. This process is additionally intensified by a heat resulting from the fact that the composite structure acts as an electrical insulator. The giant discharge partially dissipates in the form of heat, reaching, in the most extremal cases, the temperature of up to several thousands of centigrades. The resulting heat flux initiates pyrolytic processes such as local decomposition and vaporization of the polymeric matrix as well the ablation of the reinforcement, and even the ignition of the structure.

In order to overcome the problems caused by lightning strikes affecting composite elements, various lightning strike protection (LSP) solutions have been developed over the last decades. From a variety of LSP solutions one can mention several groups: coatings of metallized sprays or paints, impregnation of metallic meshes and foils as well as solutions based on dispersion of metallic particles, graphite and carbon nanostructures. Detailed overviews of these solutions can be found in. An alternative approach to LSP of composite structures has been recently developed at the Silesian University of Technology. The approach developed utilises intrinsically conductive polymers (ICPs) as a conductive filler of a carbon fibre-reinforced polymeric (CFRP) structure. In order to evaluate the effectiveness of this material, it is necessary to compare the novel and existing LSP solutions. The comparison of electrical and mechanical properties of such solutions as well as processibility of components, manufacturing complexity and operability in conditions typical to the aircraft ground and in-flight cycles is the main goal of the presented study. Additionally, the analysis of aerospace standards and requirements regarding LSP systems was performed with a special

focus on the properties of the material developed. The results obtained to date allow considering the developed LSP solution as a promising alternative to the currently applied solutions.

Organic conductive composite

The idea of development of a fully organic conductive composite resulted from analysis of existing LSP solutions, both the ones currently applied (e.g. expanded metallic meshes and foils in the newest passenger aircraft, namely Boeing® 787 Dreamliner and Airbus® A350 XWB) as well as prototypical ones (e.g. polymeric composites with metallized reinforcing fibres, dispersed metallic and non-metallic particles). The results of the analysis show that the existing solutions have several drawbacks, e.g. the LSP solutions based on the impregnation of metallic meshes and foils, despite their high effectiveness in LSP, significantly complicate the manufacturing process of such composite structures, and, additionally, increase the mass of an aircraft as the whole fuselage should be covered with a metallic mesh or foil. Moreover, due to generally low adhesion on the metal-polymer interface, debonding may occur leading to internal structural damage. If structural damage appears, the interaction of the metallic mesh with the environment may initiate corrosion processes in metallic inserts leading to the propagation of the existing damage. Other LSP solutions used today, such as metallized paints and sprays for covering composite structures, are usually not effective in the case of high current discharges due to low thickness of the coating and a low content of conducting particles incapable of forming conducting paths properly. The novel solutions developed over the last decade, have sometimes purely scientific meaning (e.g. solutions that rely on dispersion of carbon nanotubes) since the manufacturing costs of such structures are too high to apply them in practice.

In view of the above and to avoid the mentioned drawbacks of various LSP solutions, the following assumptions were considered during the development of the organic composite:

- the material should not contain any metallic inserts in order to avoid weak adhesion on the metal-polymer interface and hold a structure lightweightness,
- in order to hold the lightweightness a conductive filler from a group of ICPs should be chosen,
- selected ICP should be widely available and should be characterized by a simple and low-cost synthesis process,
- the content of ICP conducting particles should reach a compromise between mechanical and electrical properties so that the resulting material is characterized by good electrical and mechanical properties,
- the manufacturing process should be low-cost if a conductive composite structure is to be a substitute for currently used LSP solutions.

The organic composite was manufactured in compliance with the above considerations from epoxy resin (due to its good mechanical properties and a wide applicability for manufacturing in aircraft composite structures) and polyaniline (PANI), an ICP which fulfils all the mentioned requirements and is characterized by conductivity on the level of semiconductors, which consists of a matrix of a composite structure with additional dopants, solvents, hardeners, etc. The content of PANI was assumed based on numerical simulations using the percolation theory as well as conducted during the manufacturing of specimens. In order to obtain the required mechanical strength and stiffness a carbon fibre reinforcement was impregnated into the obtained polymeric mixture. The presence of carbon fibre (fabric, cloth) plays an additional role: the conducting paths in the material resulting from a formed percolation cluster were additionally supported by the impregnated fibre which also has an ability of conducting electrical current.

Requirements for LSP solutions and comparative studies

The most specific recommendations regarding LSP are given by the Society of Automotive Engineers (SAE) aerospace recommended practices (ARP) and several U.S. military standards (MIL-STD). The two main industrial recommendations are SAE ARP 5412A and SAE ARP 5414A. These recommendations are used as the basis for U.S. Federal Regulations applicable worldwide. The second of the mentioned SAE ARPs defines specific zones of lightning strikes on a typical strait-wing jet aircraft. To each of the 6 defined zones, a specific lightning current waveform is attributed (defined in the first one of the mentioned industrial recommendations). The highest current values (up to 200 kA) are attributed only to small areas, namely the nose, wings and stabilizers tips and the front parts of turbine housings, while the most of the fuselage belongs to the second zone, where the current values are much lower (up to 2 kA). Following this, LSP solutions can be applied locally depending on a specific lightning zone. In consideration of the above recommendations as well as additional recommendations related to testing and certification of lightning effects, aircraft manufacturing companies develop their own LSP controlling systems and testing procedures applied after the lightning strike event. Those should comply with the following U.S. Federal Regulation procedures:

- Systems Lightning Protection – 14 CFR 25.1316, which encompasses both direct effects and indirect effects of a lightning strike,
- Fuel Systems Lightning Protection – 14 CFR 25.954 and 25.981, which also includes direct and indirect effects,
- Lightning Protection – 14 CFR 25.581, which includes lightning direct effects,
- Precipitation Static – 14 CFR 25.899(a)(3).

In Europe, these regulations were standardized by the European Organization for Civil Aviation Electronics. An overview of the EUROCAE standards related to the mentioned SAE ARPs can be found in. The mentioned documents, however, do not provide any requirements related to materials and their properties. However, the higher conductivity of a stroked structure is the less extensive damage appears. Following internal regulations of aircraft manufacturers, defined similarly to the foreign object damage (FOD) maintenance and inspection procedures, where the threshold is determined by barely visible impact damage (BVID) and visible impact damage (VID), characteristic thresholds for lightning strike events were determined. These regulations and statistical data indicate that the lightning current discharges in the range of 5-10 kA are the most common.

In order to perform qualitative evaluation of the properties of the newly developed composite material and its adequacy to applicable standards and requirements it was necessary to compare this material and other LSP solutions using the following criteria: electrical λ and thermal σ conductivity, density ρ, ultimate tensile strength *UTS*, complexity of a manufacturing technology, and costs of a given LSP solution. Table 1 presents the materials used in LSP solutions and their physical properties important for LSP of aircraft structures, while Table 2 presents the analysis of manufacturing technologies, related costs and effectiveness of selected LSP solutions. Note that values in Table 1 should be considered as indicative only.

Table 1. Comparison of properties of materials used in LSP solutions

Material	λ, S/m	σ, W/m·K	ρ, kg/m^3	*UTS*, MPa
Aluminium	38200000	205	2690	110
Copper	59800000	401	8930	220
Graphite	72700	168	2250	24-110

CFRP	29.3	11.8	1520	350-600
CNT-reinforced composite	100000	0.2-0.25	1400	1200
Composite with metallized fibre	750-10000	414	2400-5100	650
ICP-based composite	100-50000	10.9	1521	300-800

Table 2. Manufacturing technologies and costs

LSP solution	Manufacturing technology	Costs of LSP	Effectiveness of LSP
Highly conductive metal coatings	Simple (metallized paints or sprays)	Low	Low
CFRP structure	Standard manufacturing process	Low	Very low
CNT-reinforced composite	Simple (possible difficulties with dispersion of CNTs)	Very high	Excellent
Composite with metallized fibre or immersed metallic meshes/foils	Complicated (fibre metallization, metal-polymer adhesion)	High	Fine
ICP-based composite	Simple (possible difficulties with dispersion of CNTs)	Medium	Fine

Although CNT-reinforced composites have excellent properties with reference to LSP and require a simple manufacturing technology, the costs of materials are too high to apply them in LSP on an industrial scale. Further analysis of the results presented above shows that the proposed LSP solution (ICP-based composites) have physical properties comparable with those of composites with metallized fibre of immersed metallic meshes or foils, but have, due to their organic nature, significantly lower density and require anmuch simpler manufacturing technology. Following the performed analyses and regulations of LSP, the developed organic conductive composite can be considered in future as an appropriate candidate for alternative LSP solution to be used in aircraft structures.

Summary

This study focused on the comparative analysis of physical properties and manufacturing technologies of various LSP solutions, including the developed organic electrically conductive composite in the light of technical and economical effectiveness of their applicability in protection of aircraft structures. The analysed regulations and standards as well as comparative studies show that the developed composite can be considered as a promising candidate for a LSP solution for aircraft structures due to its good strength-to-mass ratio, acceptable electrical and thermal conductivity and low-cost manufacturing process. Further studies will be focused on improvement of physical and processing parameters of the developed composite.

INVESTIGATIONS IN MILITARY AVIATION

1 STRUCTURAL LOAD / USAGE / HEALTH MONITORING

1.1 Operational Load Monitoring for Su-22UM3K twin-seated jet fighter – bomber

In many cases, aircraft operate long beyond originally specified retirement times – as long as they can effectively perform their mission and are economically viable to operate. However, keeping an aircraft airworthy requires additional engineering analyses and tests and an adequate maintenance plan to retain operational safety and reliability has to be devised.

Su-22 is a variable-sweep wing fighter–bomber, which has been used in Polish Air Force for over three decades. In 2014 the decision was made to retain a part of the aircraft population in service and increase their lifespan for next ten years, for both single- (Su-22M4K) and twin-seated version (Su-22UM3K).

Twin seated Su-22UM3K is used for training new pilots as well as maintaining good flight habits in the more experienced crew. As a consequence, this aircraft version is subject to a higher loading spectrum both during flight and landing. To ensure a high operational safety of the aging aircraft, Operational Load Monitoring (OLM) System was designed and implemented on-board for real time strain measurement of some critical structural elements. The OLM System purpose is to assist twin-seated Su-22UM3K operation and enable their controlled and safe utilization within the period of extended service life (beyond 3000 flight hours and 4000 landings).

The principal element of the OLM system is an airborne multi-role recorder with integrated data acquisition, which manages acquisition and archiving of signals coming from a permanently bonded strain gauge sensor network. Based on the data from the OLM system, periodical analysis of aircraft structure loads is performed on each aircraft and conclusions regarding the future operational usage can be drawn.

Block diagram of the OLM system is presented on figure 1. The SSR-500, manufactured by Curtis Wright Control Avionics & Electronics serves as the data acquisition unit. The SSR-500 contains 8 analog channels for strain gauges, as well as built-in test user modules. Currently, two user slots are filled with dummy modules, and are ready to use in the future for any needed sensor types and measurement tasks.

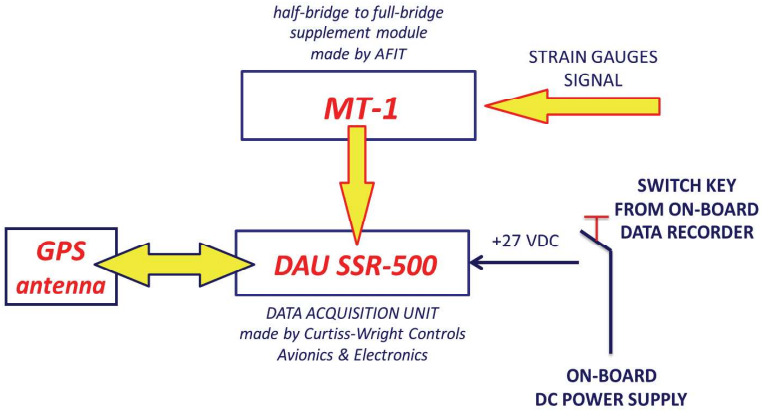

Figure 1. Block diagram of OLM system

MT-1 is a custom-made and certified additional unit for strain gauge bridge completion as well as for shunt calibration of measurement channels of the SSR-500 DAU. Additionally, the system is equipped with GPS module for time synchronization and simple navigation data acquisition.

The main data source for the OLM is an integrated network of 8 strain gauges, installed on predefined structural "hot spots" for monitoring of operational loads both during flight and landing (figure 2).

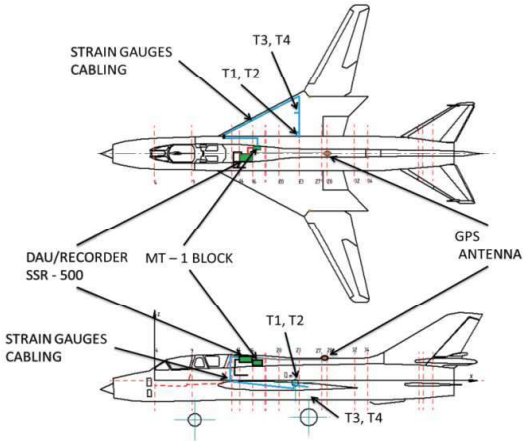

Figure 2. OLM System components on-board of Su-22UM3K jet aircraft

A pair of strain gauges is bonded on bottom and top flanges of the main wing spar, near the wing-fuselage joint. Signals from those sensors monitor load during flight and also are empirically correlated with vertical acceleration *nz* of the aircraft. For exceedances during landings, one sensor is installed on main strut to measure longitudinal loads, and one sensor is installed on the gear-wing attachment to measure lateral loads. Sensors are installed symmetrically on both sides of the aircraft to be sensitive to asymmetrical loading as well as for redundancy. Main components, SSR-500 and MT-1 are located on the top of first technical hatch (figure 3).


a)

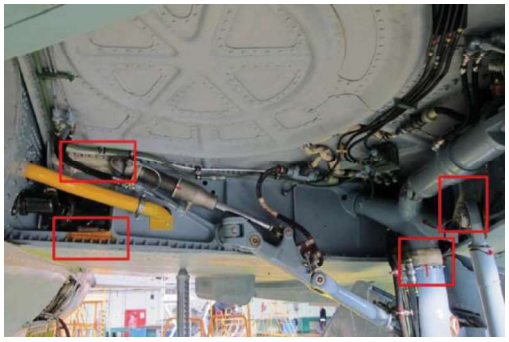
b)

Figure 3. OLM components view on-board a) data acquisition unit b) strain gauges

Beside the 8 analog strain gauge channels, the system also acquires 18 additional parameters:

- 8 built-in test parameters – e.g. internal chassis temperature, voltage values on internal power buses of data acquisition unit, power-on counter, time-on counter;
- 3 chassis parameters – day of year, StatusIn, Error counter;
- 7 GPS parameters – e.g. longitude, latitude, altitude, horizontal velocity, course, number of satellites;

All parameters are sampled simultaneously at a 16 Hz sampling rate and stored on a high capacity Compact Flash card for robust data download and transfer.

Figure 4 presents example data from a single flight. Data collected from individual aircraft are periodically analyzed to search for operational exceedances during flight and landing (e.g. high g maneuvers, harsh landings) as well as to determine true, equivalent usage per flight hour. Operational limits are determined for each individual aircraft based on electrical and mechanical strain gauge calibration, correlation with vertical acceleration and flight regime restrictions.

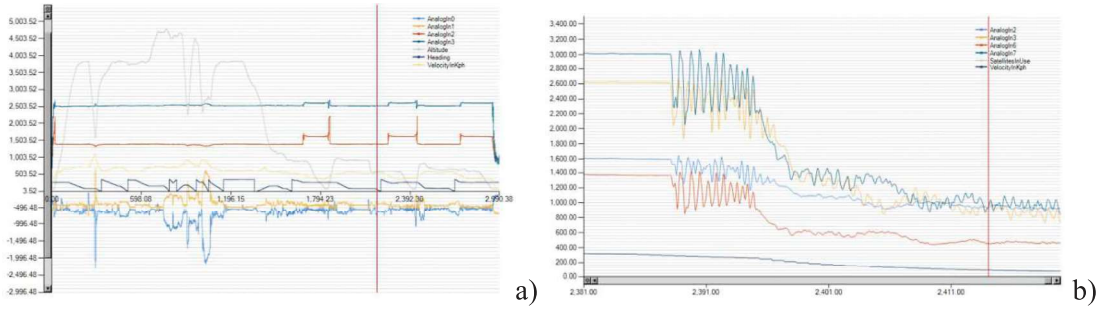

Figure 4. OLM system data example a) single flight b) strain gauges

Presented OLM System has an open and modular architecture, and modifications in both number and type of measuring channel/sensor can be easily made. Due to this fact, some future improvements for the OLM system are possible. Introduction of a triaxial, high bandwidth MEMS accelerometer installation to enhance harsh landing determination is one of the proposed modifications.

1.2 Damage identification in aircraft composite structures: A case study using various non-destructive testing techniques

Composite structures have been becoming increasingly popular especially in the aerospace industry because of their unique properties, such as excellent strength/weight ratio, corrosion resistance and a possibility of manufacturing elements of complicated shapes. However, in order to ensure a structural integrity and safety of composite elements of an aircraft they should be tested periodically during the operational life. Considering the fault-tolerant control of the structural elements of aircraft practiced nowadays by the most aircraft maintaining and service companies, the evaluation of structural integrity, evolution of existing damage and residual life of structural elements has a key importance in their maintenance. Several NDT techniques have been developed for composites diagnostic purposes. The current study was performed to investigate the performance of various NDT techniques during inspection of

aircraft composite structures, including: ultrasonic scanning (UT), thermographic inspection, PZT-based inspection and the vibration-based damage identification technique based on non-contact acquisition of modal shapes of vibration of a tested structure and their further processing.

Different types of composite structures were investigated. The first tested structure was manufactured in the form of a GFRP laminated composite using the prepreg technology with Heatcon control unit and heating blanket. This method provides only underpressure down force and one side heating, nevertheless this method is often used in Composite Patch Bonded Repair and guarantees material properties assuring safe operation. Unidirectional glass–epoxy prepreg tape was used. The stacking sequence of the layers was [0,45,-45,0,0,-45,45,0]. The structure was equipped with PZT transducers capable to actuate elastic waves. The transducers were deployed during the manufacturing process in the symmetry plane of the specimens that is between 0–0 prepreg layers. PZT discs with manufacturing code SMD05T04R111WL made by STEMINC Inc. were used. Their diameter is 5 mm and the thickness is 0.4 mm. The multiple low-velocity impact damage was introduced in the structure with an impact energy of 3, 6 and 9 J. The second investigated structure

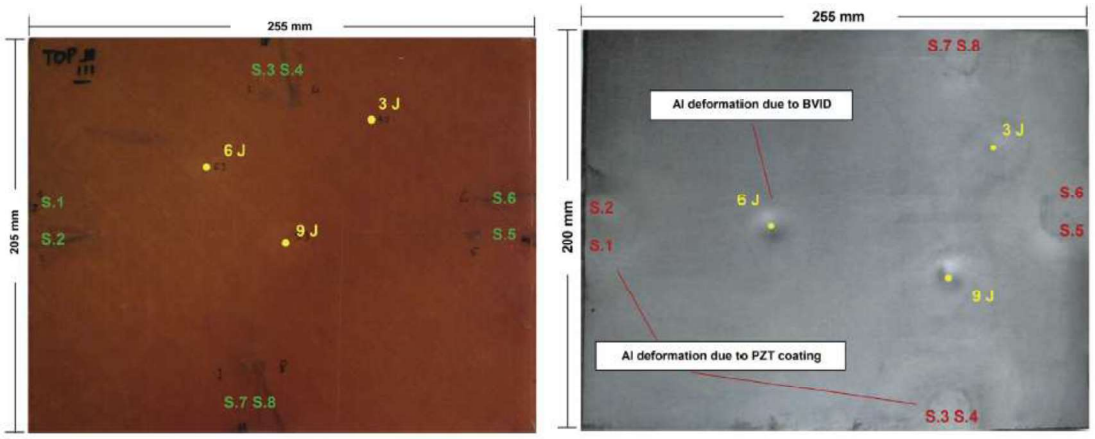

Figure 5. Composite structures tested with different NDT techniques

was manufactured as a Al-GFRP-Al metal-polymer composite with a core of GFRP laminate prepared with the same technology and same parameters as the previous one. The aluminum alloy sheets were adhesively bonded as facing sheets to the GFRP core. Due to high conductivity of aluminum alloys, the transducers were isolated before the embedding. The applied coating introduced a slight deformation of Al alloys during the manufacturing process. Low-velocity impact damage was introduced similarly as in the case of GFRP structure.

Results of inspection using PZT transducers and ultrasonic inspection

The performed experimental study considered the inspection of GFRP and Al-GFRP-Al structures using PTZ transducers embedded during the manufacturing process. Before the impact damaging and after each impact loading the series of signals were collected from each of the deployed PZT networks. The idea of damage detection relies on comparison of the acquired signals for the initial and the damaged state of the structure. In particular, it means that only a new damage of the structure can be detected and this is one of the main drawbacks

of this method comparing to classical ultrasonic testing. The data collected for the initial condition of the structure is called baselines. Baselines are needed due to the complexity of signals. In the case of UT method usually the material is tested through its cross-section under the location of a probe, using very short acquisition time and high frequencies. Thus for undamaged structure there are essentially two main signal components: first comes from the surface on which the ultrasound probe is placed and the second is the resultant echo of elastic wave reflected from the opposite surface of the examined structure. All of the wave scatterings coming from other possible boundaries can be easily extracted since they appear later in the probe. When the structure is damaged, e.g. delaminated, an additional signal component is present between the described echoes, thus the structure at a given location of the probe can be examined without any prior preparation like baselines collection. The position of PZT transducers embedded in the structure is permanent, thus in order to detect damage in a broad area the acquisition time needs to be much longer. In that case the nature of elastic wave propagation is multimodal, i.e. at a given excitation frequency there can exist many elastic wave modes with different propagation speed – the so called Lamb waves. Moreover, in real structures there exist many structural wave scatterers, e.g. rivets, joints or edges introducing additional difficulty. However the main advantage when using PZT transducers networks is that they can continuously monitor the health of the structure potentially even in flight as an on-board aircraft subsystem. Due to complexity of signals, for structure assessment based on PZT networks the so called Damage Indices (DIs) are used. The Damage Indices obtained for the two specimens for different energies of impact are presented in Figure 6.

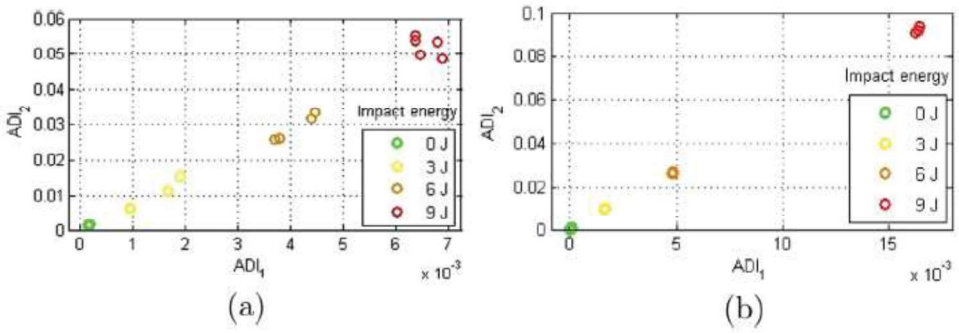

Figure 6. Results of structure monitoring with PZT transducers: (a) for GFRP structure and (b) for GFRP-Al-GFRP structure

For the ultrasonic inspection an automated MAUS® device of the Boeing company was used. System enables ultrasonic data (Time of Flight (ToF) and amplitude peak location) capturing basing on selected signal gates. The results of the inspection can be visualized in the form of C-scan mapping representing a chosen signal feature, e.g. the amplitude or ToF of a peak, with respect to the position of ultrasonic probe. On this basis damage can be identified and characterized. Signal amplifier enables data generation within the frequency of 1-20 MHz with single sensor as well as Phased Array technique. For the purpose of the inspection, 5 MHz single transducer was used. Practically the selected frequency is the trade-off between sensitivity and structure attenuation which is relatively high for epoxy composites structures. For the C-scan mapping there is a possibility to select a single step
(X-Y) resolution for enhancing images resolution or fast inspection purposes. The MAUS system enables creation of the image resolution from 0.01'' up to 0.1''. The results of UT scanning are presented in

Figure 7.

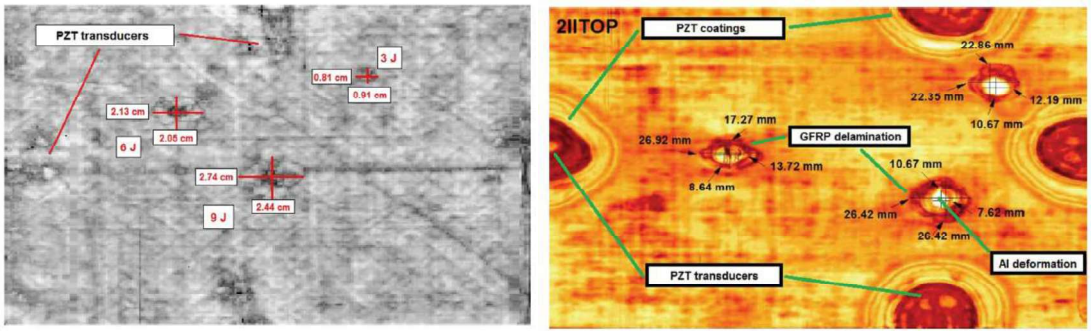

Figure 7. Results of ultrasonic testing:
(a) for GFRP structure and (b) for GFRP-Al-GFRP structure

Results of thermographic inspection

For the thermography inspection Echo Therm System of the Thermal Wave Imaging company with FLIR SC 7000 IR camera was used. As for an active thermography a very short thermal pulse is excited with use of xenon lamps excitation. The heat is transferred through the cross section of a structure from the expose surface to the opposite one. When it enters a barrier, e.g. delamination, the transfer is stopped and a damaged region has elevated temperature. This can be observed on thermograms acquired by fast IR camera. For the purpose of the inspection the following parameters were used:

- IR camera operation frequency – 54.71 Hz;
- Camera resolution – 320 - 240 pixels;
- Excitation Energy – 5 kJ;
- Wavelength – 1 - 5 x 10^{-6} m;
- Time of thermal excitation – 4 ms;
- Time window for thermograms acquisition – 5 s.

The thermograms obtained for the tested structures are presented in Fig. 8.

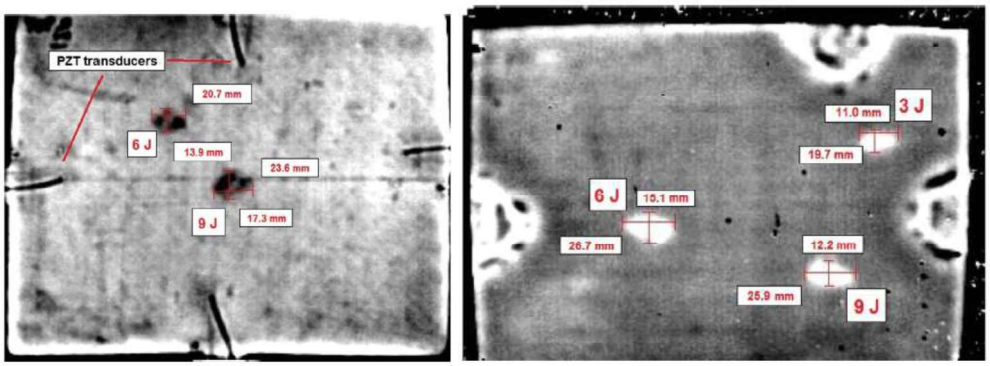

Figure 8. Results of thermographic inspection:
(a) for GFRP structure and (b) for GFRP-Al-GFRP structure

Results of vibration-based inspection

The tests were performed on all considered structures. A general idea of the testing procedure was to perform the modal analysis of a structure in order to determine the frequency response functions (FRFs) and basing on them acquire the modal shapes of vibrations corresponded to the natural frequencies of a structure. The accuracy of damage detection and localization is dependent on the number and distances between the measurement points. In the second step the modal shapes are analyzed using the advanced signal processing methods (e.g. wavelet transform) in order to determine the singularities in the modal shapes and thus the locations of a damage. The tested structures were clamped in the stiff steel frame on two opposite sides. The clamping frame limits the scanning area of 5 mm from each side. The frame was bolted to the electrodynamic shaker TIRA® TV-51120 connected with the power amplifier TIRA® BAA 500. The measurements of vibration velocity were performed by two laser Doppler vibrometers (LDV). The scanning LDV Polytec® PSV-400 was used for the measurement of velocity of displacements in the net of measurement points defined on the surface of the plate, while the point LDV Polytec® PDV-100 was focused on the clamping frame and used for obtaining the reference signal. The scanning LDV was connected with a vibrometer controller Polytec® OFV-5000 with built-in velocity decoder and a PC. The excitation pseudo-random signal was generated directly from the vibrometer-dedicated software. Collected modal shapes were then analyzed using two-dimensional (2D) single-level Undecimated Discrete Wavelet Transform (UDWT). The results of specimen testing by means of vibration-based inspection are presented in **Figure** 9.

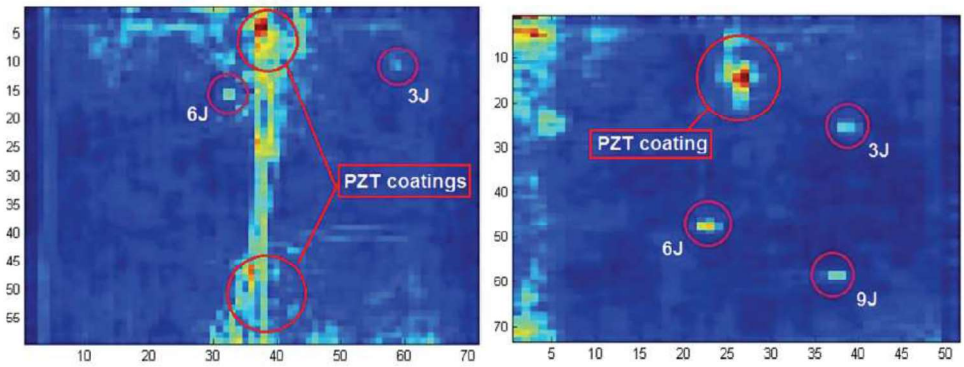

Figure 9. Results of thermographic inspection:
(a) for GFRP structure and (b) for GFRP-Al-GFRP structure

Conclusions

Performed experimental studies covered four NDT techniques used for identification of BVIDs and delaminations in aircraft composite structures. The PZT sensing technique was used for detection BVIDs in a GFRP structure and a hybrid Al-GFRP-Al structure. The analysis of results was performed using the developed damage indices and has shown comparatively good detectability of damage. This technique, however, cannot be used as a NDT tool for precise damage characterization when using low number of PZT transducers. The application of this technique is limited to rough condition monitoring of composite structures and could be considered as an initial step to the inspection of structures. The same structures were tested using ultrasonic scanning and pulsed thermography. Both techniques have revealed great effectiveness in detection and localization of introduced impact damage. However, the thermographic technique was not able to detect the damage of the lowest impact

energy in the GFRP structure. Although ultrasonic technique provides more detailed damage evaluation, e.g. depth, size and the location, especially for multilayered structures like Al-GFRP-Al, thermographic inspection is faster to be performed. This is confirmed basing on in-service experience of AFIT in testing composite elements of aircraft. The last applied technique was based on extraction of modal shapes of vibrations of tested structures and extraction of the damage presence and location using wavelet transform. This technique has given satisfactory results, but worse than by the previously discussed techniques, what was reasoned mainly by the poor resolution with respect to ultrasonic and thermographic resulted patterns.

1.3 A method to compensate non-damage-related influences on Damage Indices used for pitch-catch scheme of piezoelectric transducer based Structural Health Monitoring

About 40 years have passed from introducing nondestructive testing inspections (NDIs) as an inherent component of damage tolerant approach, in order to ensure structural integrity of aircraft. Over the years, non-destructive testing (NDT) methods became very accurate and reliable in damage detection and assessment, allowing to achieve very high level of safety in the aerospace. However, still there are some issues of this aircraft design paradigm which need to be addressed in the future. First, NDIs are scheduled based on the assumed or statistically represented loads spectrum, which does not necessarily fit to the way a given aircraft is operated. This jeopardizes the safety, but also is connected with non-scheduled inspections, whose costs are much higher than regular ones. In fact, the fraction of unexpected NDI prevails over scheduled inspections. Furthermore, application of new lightweight materials, for example, composites, introduces new damage evolution pathways, making it difficult to use low-cost NDT techniques like visual testing, which accounts for about 60% of overall NDIs. Therefore, there is a strong need from the industry sector to introduce structural health monitoring (SHM) and operational load monitoring (OLM) systems, based on sensors permanently integrated with the aircraft structure.

One of the most investigated approaches to develop SHM system is based on excitation of elastic waves by a network of piezoelectric transducers (PZTs) integrated with the monitored structure. Elastic waves can propagate significant distances, and they are sensitive to local structure discontinuities and deformations. Thus, by virtue of their nature, they can be used for damage detection, irrespective of the type of the material used for aircraft manufacturing. However, real aircraft structures can contain many elements on which elastic waves can be scattered, which results in high complexity of signals acquired by PZT. From signal *per se*, it is very hard to determine the contribution coming from damage, therefore some advanced methods of signal processing and data classification need to be applied. Moreover, the signals can be also influenced by many factors other than damage, for example, environmental conditions, degradation of the transducers' bonding with the structure, or the transducers' aging, which makes this approach to SHM particularly vulnerable to false calls. The risk of false calls of SHM systems is as much important for their application as their damage detection capabilities. A lot of studies were devoted to examine non-damage-related influences on SHM systems based on Lamb waves and to compensate the undesired effects. Most of compensation methods act on the level of the signal, that is, for a given factor influencing performance of piezoelectric transducers, signals are transformed to match the corresponding baselines. After such compensation procedure, the Damage Indices are calculated for the purpose of damage detection. In order to compensate the impact of all of non-damage-related factors, all of them need to be, at least, recognized and *for every* particular factor, a method of its compensation needs to be developed. A different technique

to compensate changes of Damage Indices values caused by factors other than damage has been proposed by the investigators. The method does not involve any operation on signals, but on the Damage Indices themselves. The factors causing Damage Indices' changes neither have to be measured nor needs to be even known. The capabilities of the method have been evaluated on the example of fatigue cracks detection in laboratory specimen tests and using results obtained during Full-Scale Fatigue Test of some components.

Signal Analysis

Structural damages can thus result in observable changes of the signal generated by the network sensors. The state of a monitored structure is assessed based on chosen signal characteristics called the Damage Indices (DIs). The acquired signals can be also influenced by factors other than damages thus posing a risk of false indications. Therefore DI's used for the structure assessment needs to be balanced between sensitivity to damages and stability under varying working conditions of transducers. In the adopted approach the DI's carries marginal signal information content. Denoting as f_{gs}^{env} the envelope of a signal generated by the transducer g and received by the sensor s and as $f_{gs,b}^{env}$ the envelope of the corresponding baseline, i.e. the reference signal obtained for the initial state of the structure, the proposed Damage Indices are given as follows:

$$DI_1(g,s) = 1 - r_{f_{gs}^{env} f_{gs,b}^{env}} \quad , \quad DI_2(g,s) = \left| \frac{\int (f_{gs}^{env} - f_{gs,b}^{env})^2 dt}{\int (f_{gs,b}^{env})^2 dt} \right| \tag{1}$$

where r_{xy} stands for the sample correlation of series x, y. Both of the proposed DI's are correlated with the total energy received by a given sensor but also with its distribution in time during the measurement. Thus the DI's are sensitive to the two main modes of guided wave interaction with a fatigue crack, i.e. its transmission and reflection from a defect.
Even such simplified damage indices can be altered over a long term, leading to the misclassification problem. Considering single sensing path, it is very difficult to distinguish whether the resultant change of DIs is caused by damage or due to such DIs decoherence. Therefore assessment approaches based on threshold levels fixed separately for DIs obtained on each of the sensing paths, would eventually lead to a false call. An alternative approach is to compare changes of DIs for all of the sensing paths. A developing damage distorts the signal only for sensing paths in its proximity. In order to decrease the misclassification risk a method to compensate such DIs drift is proposed. The method is based on the first order Taylor expansion formula and utilizes the information from all of the network sensing paths. The proposed formula reads as follows:

$$DI_{comp}(g,s) = DI(g,s) - m - (m(g) - m) - (m(s) - m), \tag{2}$$

Where

$$m = \min_{g,s} DI(g,s) \tag{3}$$

is the minimum of DIs considering all of the network sensing paths and

$$m(p) = \min_{t} DI(p,t), \qquad p = g, s \tag{4}$$

is the minimum of DIs for sensing paths originating from a given transducer p. The first subtracted term - m in the formula (2) corresponds to homogeneous DIs flow cancelation whereas the last two terms suppress the signal decoherence inhomogeneities of the generator and the sensor. The compensation formula is able to capture the drift inhomogeneities among the sensors of a network. However as it stands, it works only in a bounded interval of a given DI variability range - when its drift on a sensing path depends additively on aging of the transducers and it shouldn't be applied when this interval is exceeded. Thus simple and less volatile DIs are favored in that context.

The idea underlying the proposed DIs drift compensation formula (2) can be illustrated on the following example. Consider a 4-valent network as shown on the **Figure** 10. Suppose that the influence of uncontrolled (even non measurable) factors other than damage on a DI for a given sensing read as:

$$DI_{drift}(g,s) = \delta_g + \delta_s, \tag{5}$$

where δ_g, δ_s are the effects of those factors on the performance of the generator g and the sensor s. The parameters δ_g, δ_s might be the temperature or the pressure changes

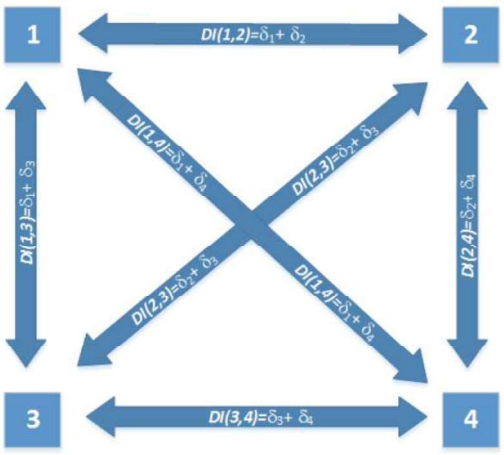

Figure 10. Damage Indices drift example for a 4-valent PZT network

on the location of g and s or combined effects of any other factors (depolarization, decrease of bonding strength) which can cause distortion of signals. The crucial assumption in derivation of a formula (3) is that the DIs drift is small. Then for compensated DIs we have:

$$DI_{comp}(1,2) = DI_{comp}(1,3) = DI_{comp}(1,4) = 0, \tag{6}$$

$$DI_{comp}(2,3) = DI_{comp}(2,4) = DI_{comp}(3,4) = \delta_2 - \delta_1, \tag{7}$$

Thus the drift has been diminished. The compensation formula has been verified in laboratory studies. **Figure** 11 shows example of DI_1 values obtain in an experiment

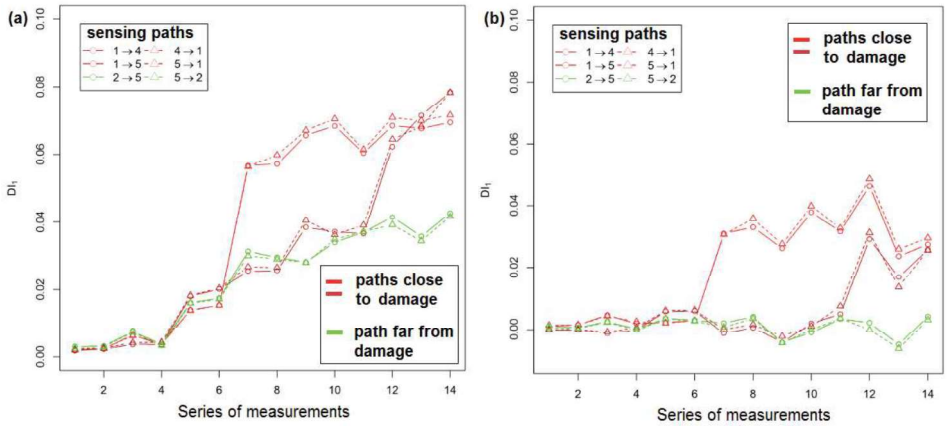

Figure 11. Example of DI_1 for sensing paths close and far from damage: (a) before compensation and (b) after compensation

in which a fatigue crack was introduced in a tested structure. Damage Index drift is visible for both – sensing paths close and far to a crack (**Figure** 11 (a)). After the compensation the drift was removed but the contribution to compensated Damage Index from the damage was maintained (**Figure** 11 (b)).

Example compensation formula application

The compensation method for PZT based SHM was used for the purpose of fatigue test of a helicopter tail boom. a helicopter tail boom. The test was a part of ASTYANAX (Aircraft fuselage crack monitoring sYstem And prognosis monitoring sYstem And prognosis through on-boArd eXpert sensor network) project governed by European Defence governed by European Defence Agency. The platform used for the project is Mi-8/17 helicopter. The tail boom of **helicopter.** The tail boom of the helicopter was equipped with PZT sensors as well as crack gauges. In the

Figure 12 a PZT network and crack gauges installed near an introduced crack are presented. Two kinds of PZT transducers were used: single- and multi-layered. The signals from PZT network were gathered under varying loads and the temperature which can contribute to the DIs drift effect.

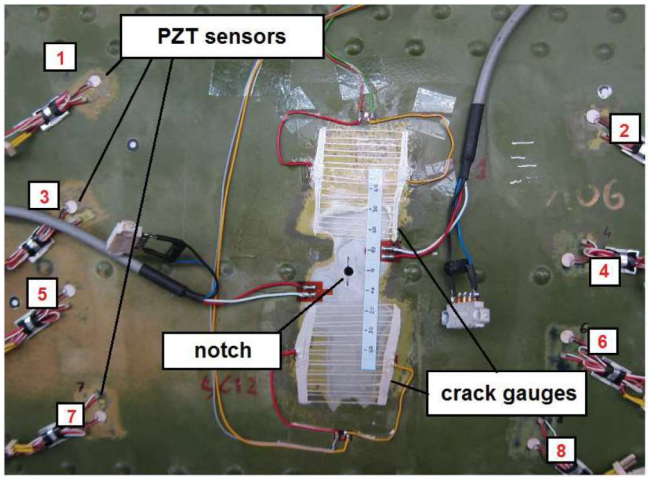

Figure 12. PZT sensors and crack gauges deployed on the helicopter structure with numeration of PZT network

In **Figure** 13 DIs change within the network before (a) and after (b) the compensation are graphically represented. The change of compensated DI is the highest for sensing paths running in close proximity of the crack (**Figure** 13(b)), whereas uncompensated DI can change also for paths for which signal should not be influenced by a damage (**Figure** 13 (a)), which can lead to a false indication of the system.

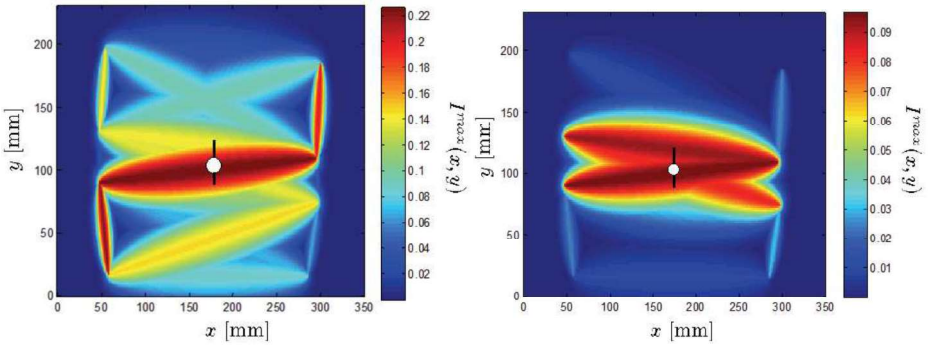

Figure 13. Visualization of Damage Index change within the network using: (a) not compensated and (b) compensated DI

Conclusions

The drift of Damage Indices (DIs) is a phenomenon resulting from many non-damage-related factors, can highly increase the risk of false calls. In practice, it can be hard to measure and fully recognize the factors driving the drift. In the proposed methods for DIs' compensation, only the DI values obtained on different sensing paths of a given network are used, without prior knowledge about factors driving the drift. In principle, the formula should be valid for all of the non-damage-related factors. Furthermore for the application of compensation formula, the factors driving the drift of DIs neither have to be measured nor needs to be even known. The efficiency of the formula was tested during several experiments, e.g. fatigue test of a helicopter tail boom or Full Scale Fatigue Test of PZL-130 Orlik TC-II aircraft.

2 FULL SCALE TESTING

2.1 The Full Scale Durability Test of the Su-22 “Fitter”

The Full Scale Durability Test (FSDT) was carried out on an out of service aircraft. During the verification process, the aircraft was prepared for the test by removing the engine, avionics, and horizontal stabilizer, canopy and wheel fairings. Moreover, the landing gear was fixed in the extended configuration. In addition, the wing main pivot joints as well as both flap sets (inner flaps in the fixed wing part and outer flaps in the sweep wing part) were inspected, since their functionality was crucial for the test.

The test specimen was shipped to the Výzkumný a zkušební letecký ústav (VZLÚ) in Prague (CZ) where the test was carried out. The aircraft structure was lifted using a gantry crane and the test rig was built around it (**Figure** 14). The structure was fixed in two locations, bulkhead No. 4 and bulkhead No. 34 (two smaller outer frames on the fuselage in **Figure** 14). Loads were exerted on the structure by means of hydraulic actuators which number varied between stages of the test. Flight and landing loads were exerted by means of actuators mounted to the wings and landing gear, while seven actuators underneath the fuselage (from front landing gear to horizontal stabilizer) allowed to distribute reaction forces. Loads on the fixed bulkheads No 4 and 34 were also monitored throughout the test by means of load sensors.

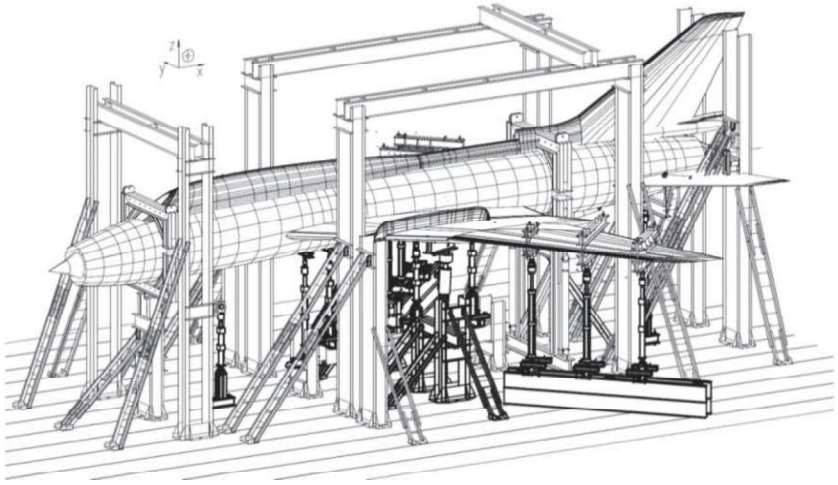

Figure 14. Test rig for Su-22UM3K durability test

Due to the variable sweep angle of the outer parts of the wing the Full Scale Durability Test (FSDT) was divided into four stages. In the first stage, in which the landing loads were taken into account, the wing sweep angle was set to 45 degrees and the whole structure was loaded by means of 16 actuators in total. Both left and right landing gear was loaded by means of three actuators, the sweep parts of the wing were loaded each by two actuators. Seven actuators were acting on the bottom of the fuselage. Load spectrum was defined based on the landing loads measured during the Operation Load Monitoring Program as well as based on the historical data. The main goal of this part of the test was to substantiate durability of 6500 landings with a safety factor 4.

In the second stage, consisting of flight loads, the outer wing sweep angle was set to 45 degrees. Six actuators loading the main landing gears were removed. Two actuators (one

each side) were mounted underneath the fixed wing parts as well as two additional actuators (one each side) were added to the sweep wing parts. Reconfiguration of the actuators allowed more complex load distribution along wings. Load spectrum for the second stage was also defined using OLM Program results and historical data gathered by AFIT.

The third part of the test was focused on the wing flap loads and necessitated a change of the outer wing sweep angle to 30 degrees, removal of the wing actuators and extension as well as locking the inner (fixed wing part) and outer (sweep wing part) flaps thus allowing the four actuators to act on the lower surfaces of the flaps. In this stage the whole aircraft structure was used as an interface (all actuators beside the flap actuators were set to level flight configuration) and the variable loads were exerted on the lower parts of the flaps by means of the four actuators. Loads for this stage of the test were calculated using flight mechanics principles. The aim of this part of the test was to prove the durability of the flaps and flap hinges – i.e. their ability to safely withstand 6500 landings with a safety factor of 4.

The test configuration in the fourth stage was identical as in the second stage; therefore wing sweep angle was set again to 45 degrees. The fourth stage was divided into two sub-stages. In the first sub-stage the load spectrum from the second stage was used – however, the lowest amplitude loads were removed. In the second sub-stage a simplified load condition varying between vertical g-force 1(level flight) and vertical g-force 6 was used. The first sub-stage was finalized without critical damage. The structure failed during the second sub-stage after approximately 5000 load cycles. Each change of the wing sweep angle throughout the test was conducted by the Military Aviation Works No. 2 JSC personnel.

Figure 15 shows graph representation of test progress for each stage of the test. Horizontal sections in Figure 15 a) and b) represent Non Destructive Inspections (NDI) carried out during the test. During the inspections minor defects were found in the non-critical elements of the structure. An example of such damage is shown in Figure 16 a), where a crack propagating from an access hole on the wing was found at 6500 SFH. The crack initiated at the hole edge and was inhibited by a screw hole. Figure 16 b) shows the critical damage of the right wing spar which cracked during the second part of stage four.

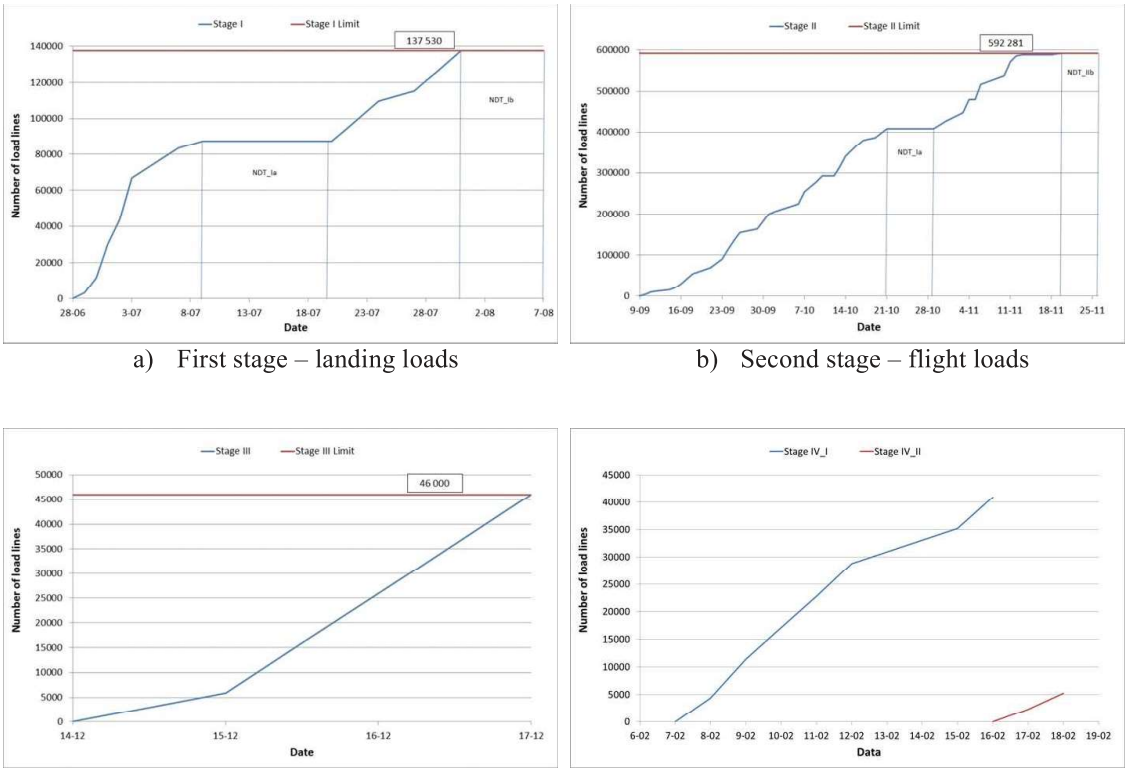

a) First stage – landing loads

b) Second stage – flight loads

c) Third stage – flap loads

d) Fourth stage – flight loads until critical damage

Figure 15. Progress graphs of for the four stages of the fatigue test

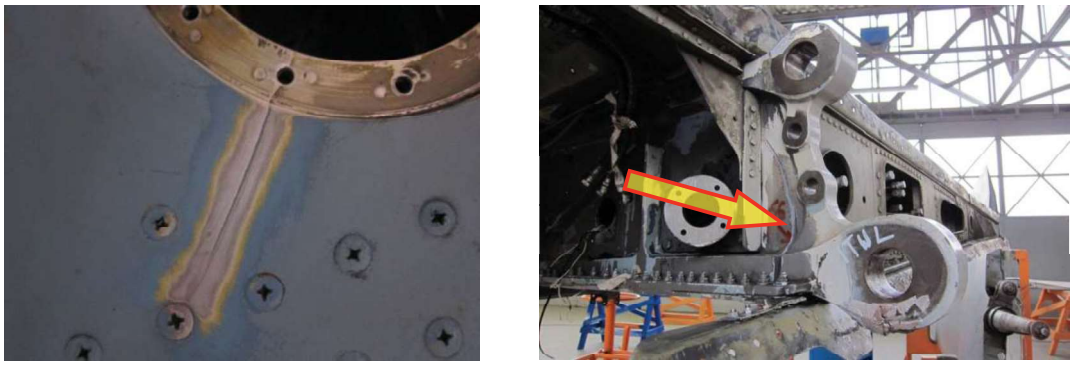

a) b)

Figure 16. Defects found during the Durability Test:
a) crack propagating from access hole found at 6500 SFH,
b) critical damage which ended the test

The results of the test have proven that the Su-22 aircraft structure is capable to be operated with the desired flight profile i.e. 800 Flight Hours after overhaul. Additionally, the test results used to define Individual Aircraft Tracking (IAT) program. The IAT is based on

vertical g-force recorded by Flight Data Recorders (FDR) – this parameter is used to estimate actual fatigue usage of each Su-22 aircraft operated in Polish Air Force.

2.2 Full scale durability test of the MiG-29 vertical stabilizer

Based on the usage and load data a fatigue test has been designed for the needs of a durability test of the MiG-29 composite stabilizer. The test will take place at the Structures Testing Subdivision of the Institute of Aviation in Warsaw. A cut-out of the back section of the fuselage serves as the mounting platform for the test object (stabilizer). The cut-out is attached to the framework of the test stand. The load is applied with the use of four actuators via two parallel clamps attached in the regions of frame 3 and 6.
In the full scale durability test, bending and torsion will be applied to the stabilizer. These will locally result in tension and compression in the spars, as well as shear in stabilizer skin. A strain gauge installation serves as the main source of information about the structural behaviour of the stabilizer – the strain gauges were installed in regions remote from the loading clamps and the composite bonded repair areas. Tension/compression is monitored by sensors installed along the spar lines, whereas strain gauge pairs in (rosette configuration) were placed on skin between spars and stringers to record shear strains.


a


b

Figure 17. View of the Full Scale Durability Test Stand

3 COMPOSITE MATERIALS & STRUCTURES

3.1 Composite bonded patch repairs in polish air force

When appropriately designed, Fiber-polymer composite patches made with the use of preimpregnate (prepreg) technology can have physical properties similar to the materials of the repaired structures. Modern adhesive films, similarly to the prepreg composites are based on thermosetting resins. The adhesive film stiffness provides high fatigue resistance for the bonding. The quality of the composite patch repairs implemented by AFIT was verified with the use of thermo-mechanical testing; as well as 3D scanning and reverse engineering methods (CAD/CAM software).

Various repair technologies have been implemented on the following aircraft:

- Su-22- crack repair of the hermetically sealed hose of the second cabin;
- PZL 130 Orlik TC-II - Reinforcement of lower wing surfaces by means of composite repair packages;
- MiG-29 - upper air intake flap.

Many of the aircraft components operated by the Polish air force have already exceeded their original design life. The traditional bonding methods such as riveting or welding are unacceptable for use in repair of critical components because material loss, as well as material change due to thermal loads can result in significant stress concentrations. Component replacement is impossible because of low part availability, therefore damage-tolerant operation as well as usage of efficient repair technology is required. AFIT was requested to address this issue.

Repair of Su-22UM3K aircraft structure

The repair of the pressurization hose frame fracture was performed by applying a composite bond repair package (PNAP) that reinforced the damaged structure. The repair was carried out with the use of prepreg technology using the HEATCON thermal cycle unit and a heating blanket. The heating process report as well as the NDI tests carried out after the repair, confirmed that the repair was carried out properly.

The designed repair package was based on a CFRP composite patch. Documentation held by the Air Force Institute of Technology does not contain detailed information about the type of aluminum alloy from which the damaged element was made. During the visual inspection of the structure after the paint coating was removed, numerous blisters and unevenness of the surface was observed - typical for sand casting manufactured components. The defect propagated from the bladder to the edge of the structure. The material data used for repair package calculations was obtained during a material strength test. The primer and the adhesive film determine the structural properties of the interface between the patch and the structure. For the purpose of the design calculations a safety factor x = 2.5 was assumed, reflecting the influence of the human factor.

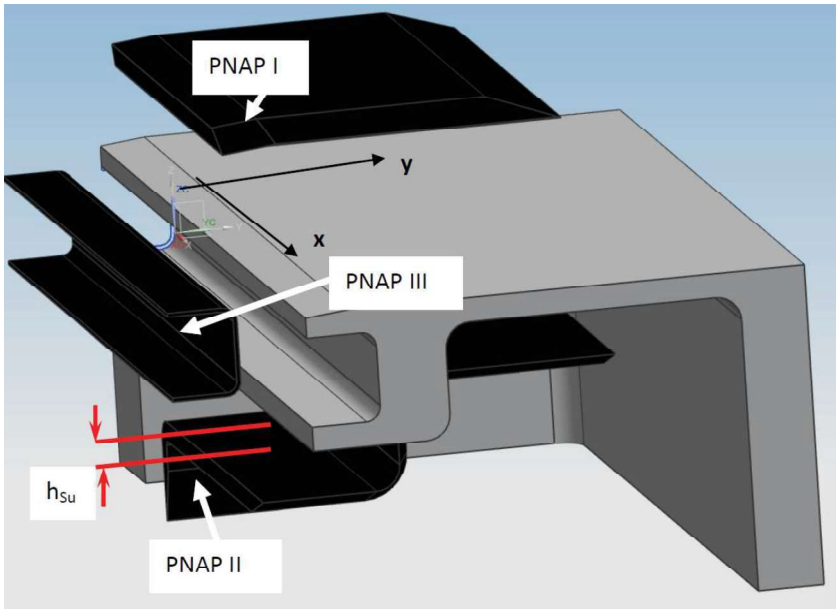

Figure 18. Structure reinforcement system using composite patch repair packages (PNAP)

Damage occurred on the lower part of the duct. The thickness of the structure at this point is 5 mm. In the calculation it was assumed that the repair is one-sided and only the PNAP II carries loads. It was also assumed that the loads act only in the X direction (Figure 18). The length of the patch measured from the damage location (X direction) was defined by taking the strength of the adhesive into account.

It was assumed that the orientation of the layers in PNAP I and II must satisfy the quasi-isotropic balance, which provided similar mechanical properties in all directions of the PNAP plane. This arrangement of fabrics is fulfilled for the following distribution of ply orientations: +/- 45° - 50%, 0° - 25%, 90° - 25%. By determining the value of the function (5), it is possible to estimate the mechanical properties of the composite in one direction.

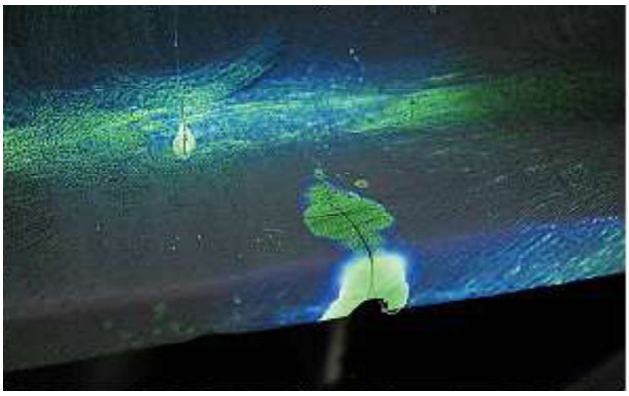

Figure 19. Fracture of sealing hose frame in the upper part of the second pilot cabin, above the seat

Figure 20. Structure after repair, sealing hose installed

Repair of structural elements of PZL-130 TC-II „Orlik"

During the full scale fatigue test of PZL-130 TC-II „Orlik" aircraft, after 19360 SFH, defects were detected in the wing lower skin. Fractures were found in the region between wing main spar and the front spar on the rivet joint near rib number 6.The repair was performed by reinforcing the lower wing skin with composite repair packages, using a HEATCON control unit and a heating blanket. CFRP and BFRP prepreg materials were used for the repair packages.

Figure 21. Location of the composite repair patches on the aircraft wing

Repair of MiG-29 - upper air intake flap

Some RD-33 engines have been damaged by rivets falling from the engine air intake upper flaps. Cost of the engine repair is high and flight safety consequences can be severe. Conventional repairs i.e. riveting were ineffective (high cycle vibration & fretting fatigue). Bonded Composite Patch Repair is an effective repair solution that mitigates the above problems. Prepreg technology was utilized (boron and Kevlar).

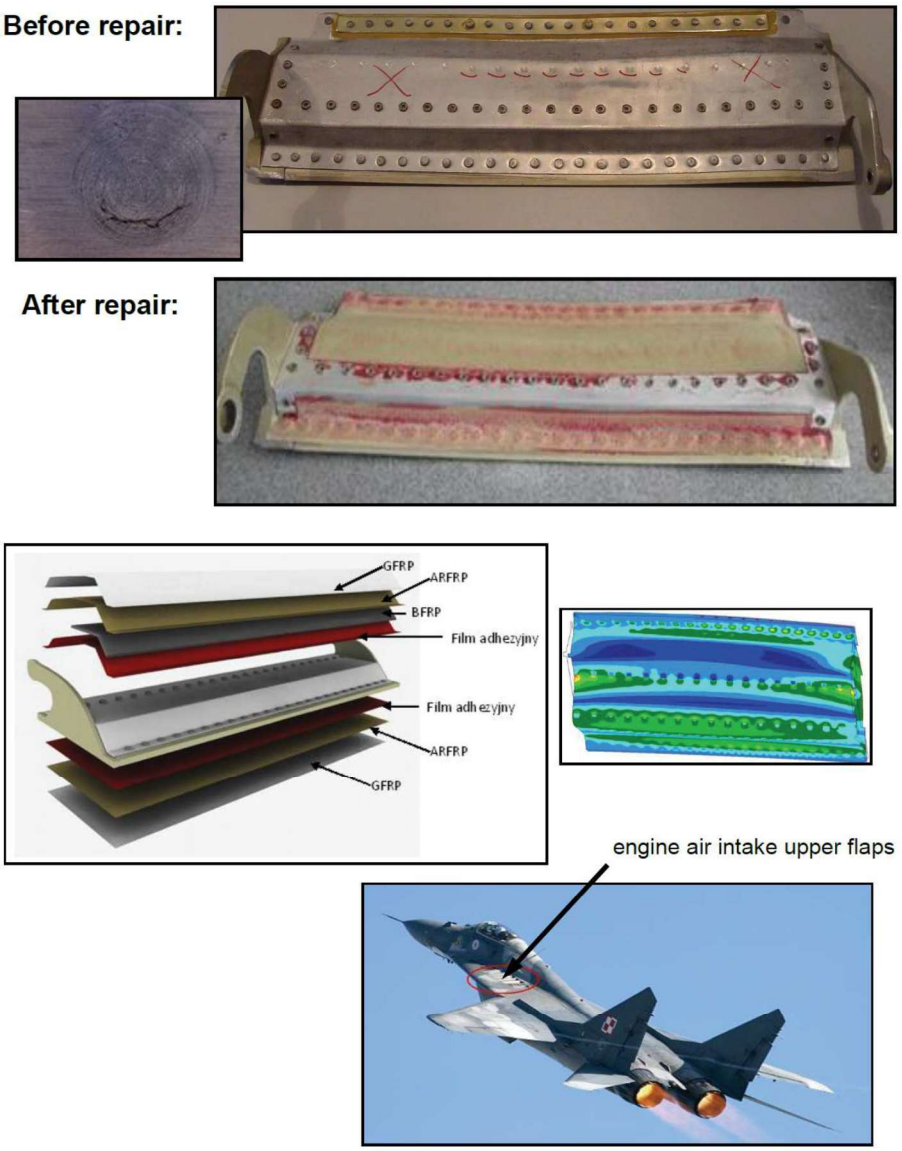

Figure 22. Overview of the repair process

4 NON-DESTRUCTIVE EVALUATION

4.1 Service Life Extension Program for Helicopter Main Rotor Blades

Polish Armed Forces fleet of helicopters is mainly based on Russian made helicopters such as: Mi-2, Mi-8, Mi-17, Mi-14, and Mi-24. The maintenance of main rotor blades (MRB) of these helicopters is based on service life. There are two service life criteria in MRB maintenance:

- service life based on hours - Hourly Service Life - HSL (measured in hours);
- service life based on time interval - Calendar Service Life - CSL (measured in years).

These criteria determine service life of MRB. Frequently, after reaching the CSL, around 60% of hourly service life remains. It means that sometimes, airworthy MRBs must be replaced because of aging (CSL). Cost Benefit Analysis suggested that a service life extension program should be implemented by the AFIT (Air Force Institute of Technology). The structure of MRBs used in Polish Air Force can by divided into two main categories: single spar/multi-section honeycomb and single spar/single-section honeycomb. The metal/multisection design is most widely used in Polish Armed Forces.

Maintenance procedures used so far were based on visual inspection, with additional support of tap testing. Those techniques are fast and fairly simple to use but not reliable and operator dependent. Therefore an additional NDT program was required. In the course of the program main NDI techniques were used, such as: Shearography, MIA, Pitch-Catch, Ultrasonic, Ultrasonic Phased Array, Eddy Current and X-Ray. These techniques were supported with PC interface, which made possible on-site as well as off-site data analysis and post-processing. Other advantages of PC based interface include: data storage and result comparison capability, automated scanning head movement, enhanced visualization. First step in the NDE program was to prepare test coupons taken from out-of-service MRBs as well as the blades in service. In these coupons it was possible to create defects analogous to the defects found in maintenance, and a detectability study was performed. Afterwards, comparison of NDT results for MRBs operated in different environmental conditions and with varying HSL/CSL was performed.

Based on service data obtained by the AFIT following defect types were determined to be the most commonly found in the MRBs:

- disbonds (skin-honeycomb, skin-spar);
- cracks (spar);
- corrosion;
- water inhibition (honeycomb cells).

Figure 23. X-Ray (left) and eddy current (right) inspection results of the crack in the main spar

Figure 23 presents the results of X-Ray and eddy current inspection of the crack location in the main spar of the blade.

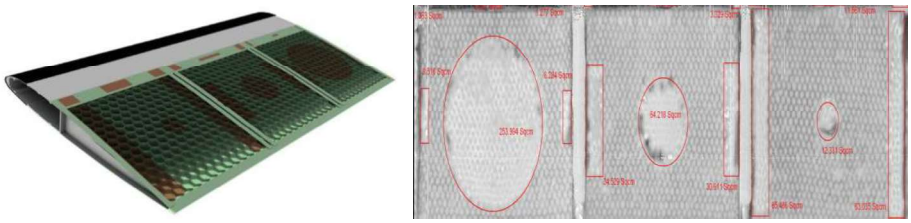

Figure 24. Calibration specimen design (left) and MIA (right) inspection results of the disbonds

Figure 24 presents capability for skin/honeycomb and section/spar disbond detection based on mechanical impedance analysis. Most of the selected inspection methods enable damage detection and damage size quantification. For most of the listed damage scenarios several tests enabling damage detection capability evaluation were performed. Based on the conclusions from the program's three years run, service inspection bulletins have been devised and introduced into service life extension programs. Currently, based on the devised NDI bulletins service life extension programs are implemented on the selected helicopter types.

4.2 Inspection Programs for MiG-29

MiG-29 is the fighter jet used in Polish Air Force. Two main criteria in the maintenance approach of MiG-29 are analogous to helicopter MRB programs and are based on HSL and CSL. Condition Based Maintenance (CBM) was implemented for selected aircraft. One of the primary tasks in the CBM implementation process was an extensive NDT (Non Destructive Testing) program for critical components, along with a corrosion inspection program.

The MiG-29 utilizes a twin vertical stabilizer design. Vertical tail consists of aluminum spars and composite skin made of CFRP (Carbon Fiber Reinforced Plastic). Skin is monolithic with thickness in range of 1.8 mm – 3.2 mm and it's bonded to the aluminum structure with the use of bolts and adhesive. Nondestructive testing of MiG-29 vertical stabilizers is focused on CFRP skin defects such as:

- delaminations - separation between layers of composite;
- disbonds - lack of adhesive;
- porosity – resin-poor areas;
- foreign object inclusions.

Techniques which are used for inspection of MiG-29 vertical stabilizer are also used for F-16 horizontal and vertical stabilizer and are presented in table below:

Table 6 – Information about NDT techniques used

	Resonance	**Shearography**	**UT**
Delamination	-	-	+
Disbond	+	+ (core-skin disbond)	+
Porosity	-	-	+
Foreign Object Inclusion	-	-	+

To perform structural integrity test of the composite vertical stabilizer ultrasonic testing was used. The total surface area for inspection was approximately 11 sq. meters per one aircraft. The aircraft population which is currently tested is more than 30. Therefore total area for inspection was more than 600 sq. meters. Classical tests with use of manual scanning were therefore inefficient and labor-intensive. Automated scanning procedure had to be applied and MAUS ®V scanning system was used. MAUS® system (Mobile AUtomated System) is a hybrid construction and makes possible inspection with such techniques as: ultrasound (including Phased array), eddy current, MIA, Pitch-Catch, Resonance. The System is fully portable and enables inspection on horizontal and vertical, as well as inverted surfaces. That is possible due to its flexible track system and suction-cup based mounting. On the Figure 25 inspection of the vertical stabilizer composite skin is presented.

Figure 25. Composite Vertical Stabilizer Inspection

Resonance and ultrasonic inspection with MAUS system are quantitative methods. Results are presented with use of C-scan imaging (amplitude and ToF - Time of Flight). Below, on

Figure 26, an amplitude C-scan of the F-16 horizontal stabilizer is presented, along a ToF C-scan of a MiG-29 vertical stabilizer. On the amplitude data, varying colors correspond with signal attenuation. Amplitude mode is useful for determination of the damage location.

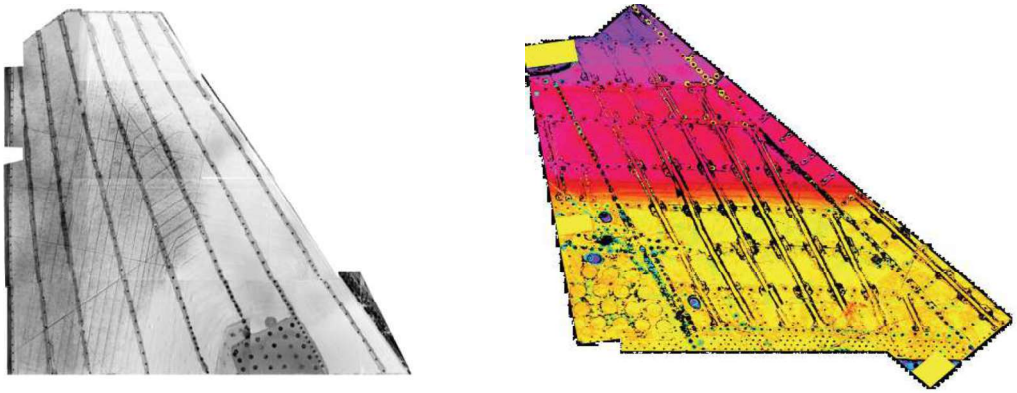

Amplitude C-scan F-16 horizontal stabilizer TOF C-scan MiG-29 vertical stabilizer

Figure 26. Example results

Color range in the ToF data gives information about different composite skin thickness as well as about depth of the delamination location. Damage location on the stabilizers has been found to have an approximately normal distribution**.**

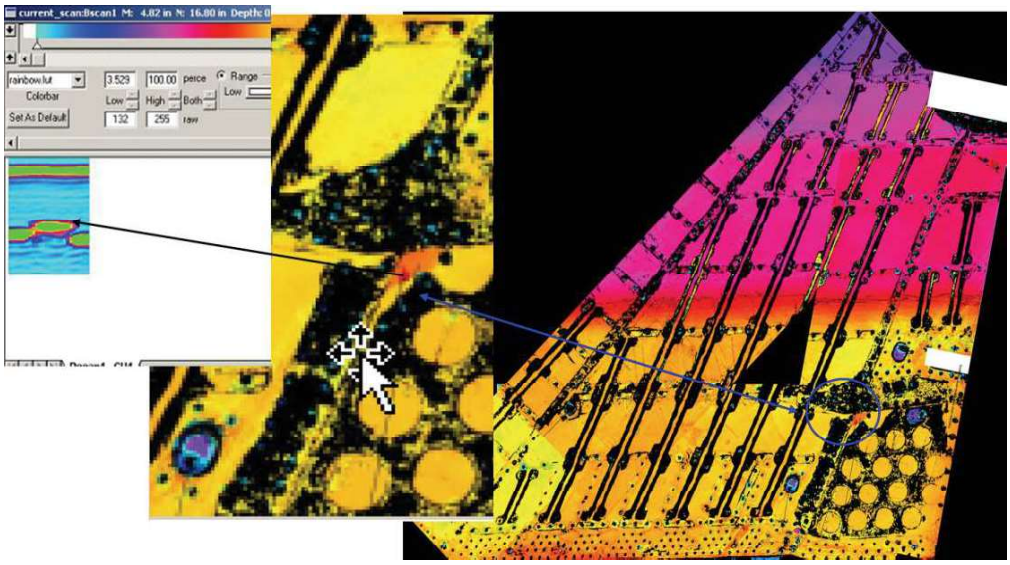

Figure 27. Foreign object inclusion (embedded) in MiG-29 vertical stabilizer

When an additional defect characterization is needed a full waveform record based on B-scan visualization (as presented on
Figure 27) is available. This type of presentation is applied for detection of delamination and foreign object inclusion. The disbond defects typically occur in the bottom part of the stabilizer. At present, monitoring has been implemented for all MiG-29s in service aircraft, under the AFIT designed service bulletins.

Monitoring of MiG-29 engine flap composite bonded repair patch

First step of NDI was performed during the manufacturing phase. The engine intake flap repair was performed with the use of a vacuum bag and heating blanket. The cure cycle was strictly monitored by the control unit. After the cure cycle non-destructive tests were performed to verify the bond quality. Main two methods used during the examination were thermography and eddy-current testing.

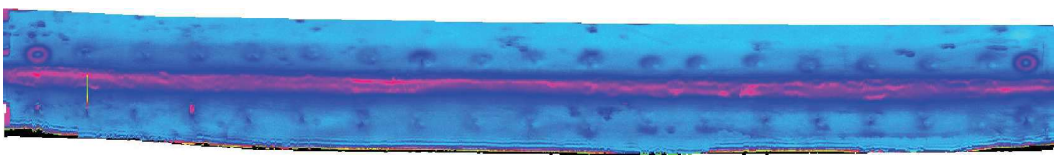

Figure 28. Result of eddy-current examination

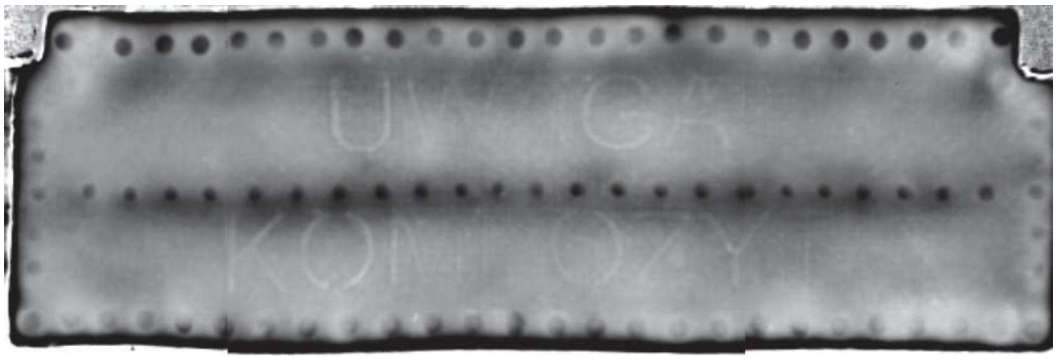

Figure 29. Result of thermography examination

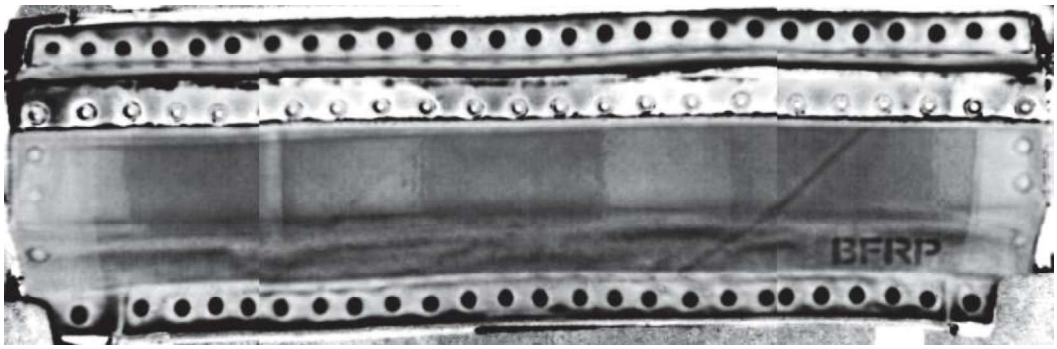

Figure 30. Result of thermography examination – bottom surface

Repaired flaps were installed on the aircraft and positively validated during flight test. At present more than 30 jets are flying with the repaired flaps. For the purpose of bond quality monitoring, service inspection bulletin was devised and implemented in the maintenance procedures.

Figure 31. Engine air intake upper flaps after modernization

5 MODELING AND SIMULATION

5.1 Simulation based determination of residual life for repaired components of MiG-29

Problem outline

Composite and metal areas of the MiG-29 aircraft control surfaces are subject to localized defects. AFIT monitors the propagation and occurrence of such defects during aircraft service. Defect monitoring is based on regular NDT inspections of the structure. Recently, a development of a repair methodology for the critical elements has been started. The repair is based on application of composite bonded patches. A research programme has been implemented to facilitate the development. The programme includes numerical simulations as well as experimental tests. Both the experimental and numerical results will aid the assessment of structural integrity and strength of the damaged and repaired components. Determination of residual strength as well as component airworthiness will be done for the following scenarios:

- component with a pre-existing defect (encountered in service),
- component that has been damaged and subsequently repaired.

To enable this assessment, several modeling techniques and solution types will be used, such as:

- buckling and post-buckling simulation;
- application of actual loads;
- simulation of defect growth in composites;
- modeling of adhesive bonds and riveted interfaces
- modeling of metal-composite interfaces;
- modeling of honeycomb structures;
- simulation of influence of environmental conditions.

Numerical simulation outline

Because of the structural complexity of the components, a multi-stage approach to model creation and validation is needed i.e. a “test pyramid” is needed to establish structural characteristics of the full scale components based on the parameters of the simplified or local models/test coupons. Simplified, local coupons are easier to analyse and test. On the other hand research based on the detailed, large-scale models is needed to verify the model assumptions for the actual structure. Combination of data gathered during simplified model testing and analysis enables the creation of a validated full scale structural model.

Because coupon cost rises with complexity, a significantly larger amount of testing is possible on the lower levels of the pyramid. The lower steps are mainly used to calibrate the model, whereas the higher steps serve for the purposes of model validation (and verification of the lower level assumptions).

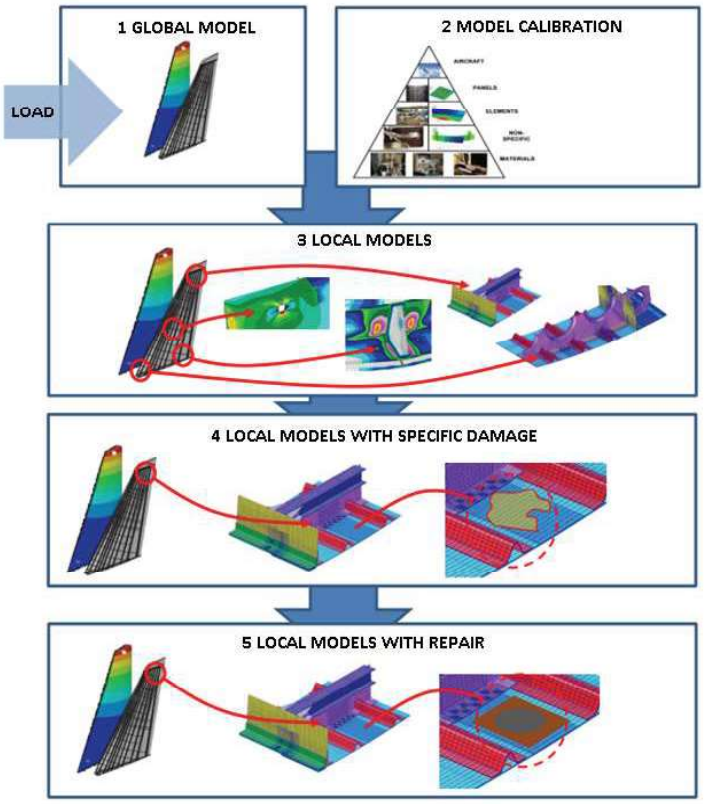

Figure 32. Idea of the test pyramid approach

Digital models, reverse engineering

Because of the limited manufacturer support and lack of detailed technical documentation in the case of MiG-29, use of reverse engineering methods was required to characterize the structure. With the use of structured light 3D scanning (GOM ATOS scanner), as well as photography based photogrammetry (GOM TRITOP system) a full geometry description of the components could be obtained.

Figure 33. Photogrammetry results – example photo and the resulting point cloud

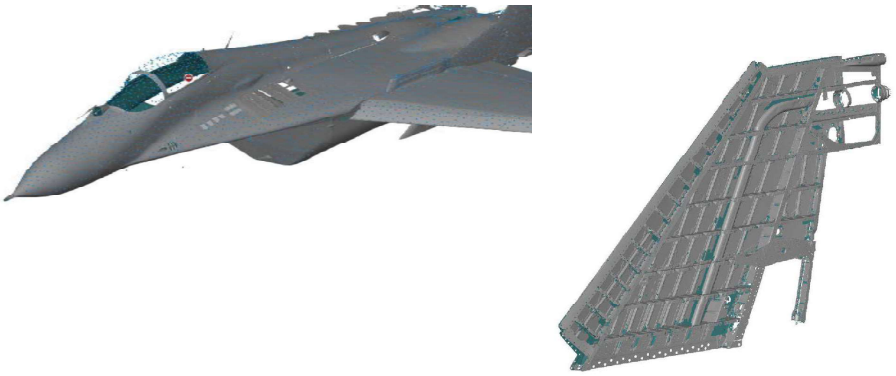

Figure 34. Examples of 3D scans used for reverse engineering

The raw geometry representation obtained with reverse engineering methods was converted to a smooth NURBS (Non-Uniform Rational B-Spline) representation with the use of CAD tools. In the end a simplified, smoothed geometrical outline of the complete MiG-29 was created (for purposes of aerodynamics modelling) as well as the detailed structural models of control components: vertical and horizontal stabilizer, aileron, wing flap and rudder. The detail of the structural models includes elements such as ribs, frames, struts and stringers.

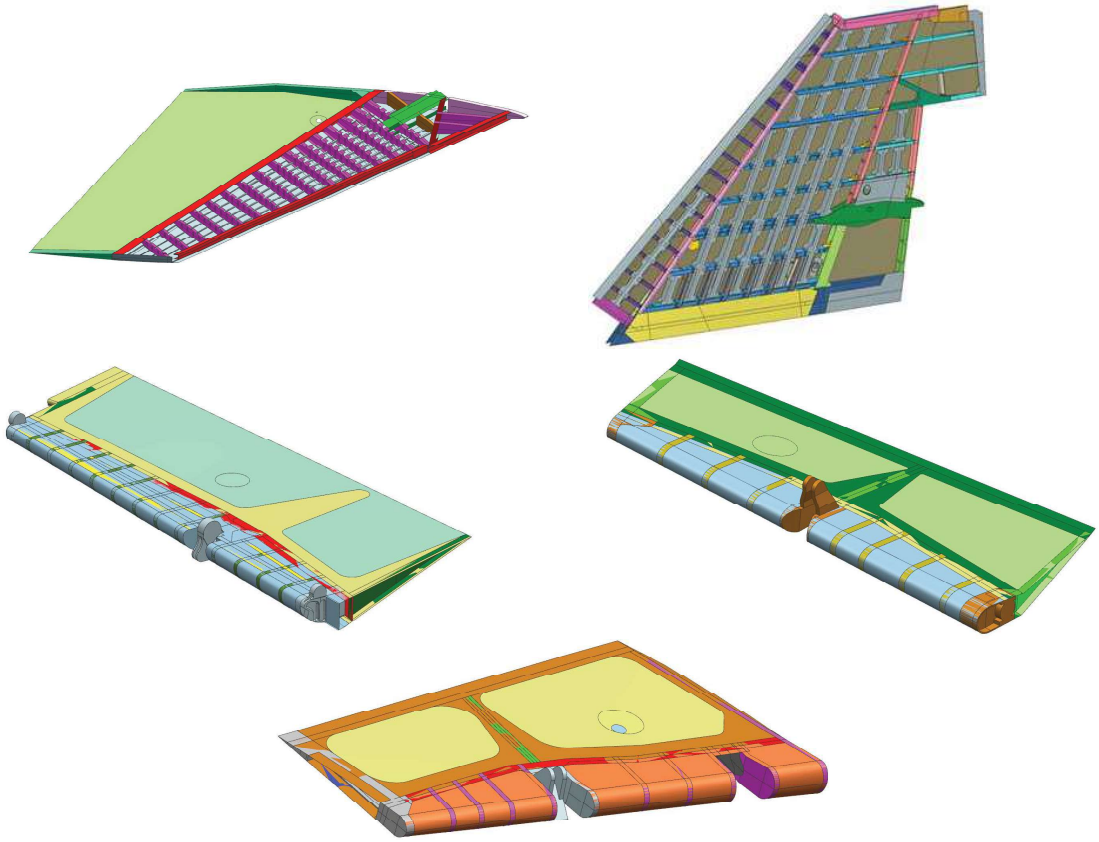

Figure 35. NURBS geometry representation – CAD model examples

Numerical models consisting of finite element meshes with structural properties applied (ABAQUS) were the end result of the reverse engineering process. These models are the basis of the numerical simulations needed to establish the damage response as well as repair durability. The model parameters will be tuned and calibrated throughout the duration of the project, based on the experimental validation results.

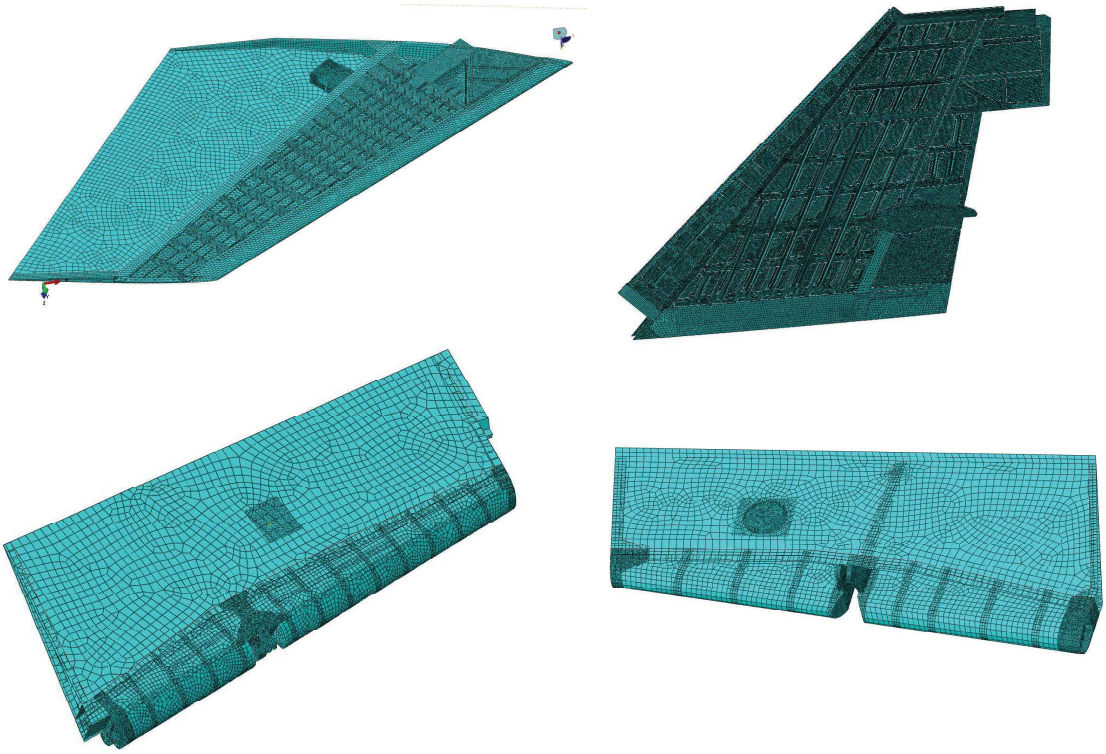

Figure 36. Numerical models – FE meshes

Structural characterization and model calibration

The determination of residual strength of repaired and damaged components requires detailed structural characterization. The test pyramid approach, described above requires that a series of coupon and full-scale mechanical tests should be performed. Especially important is the determination of fracture mechanical parameters of composite elements, in particular the delamination behaviour. Result of those tests will serve as an input for the finite element numerical simulations. AFIT has manufactured a series of coupons that correspond to structural elements of the analysed components, with varied level of detail corresponding to the levels of the pyramid.

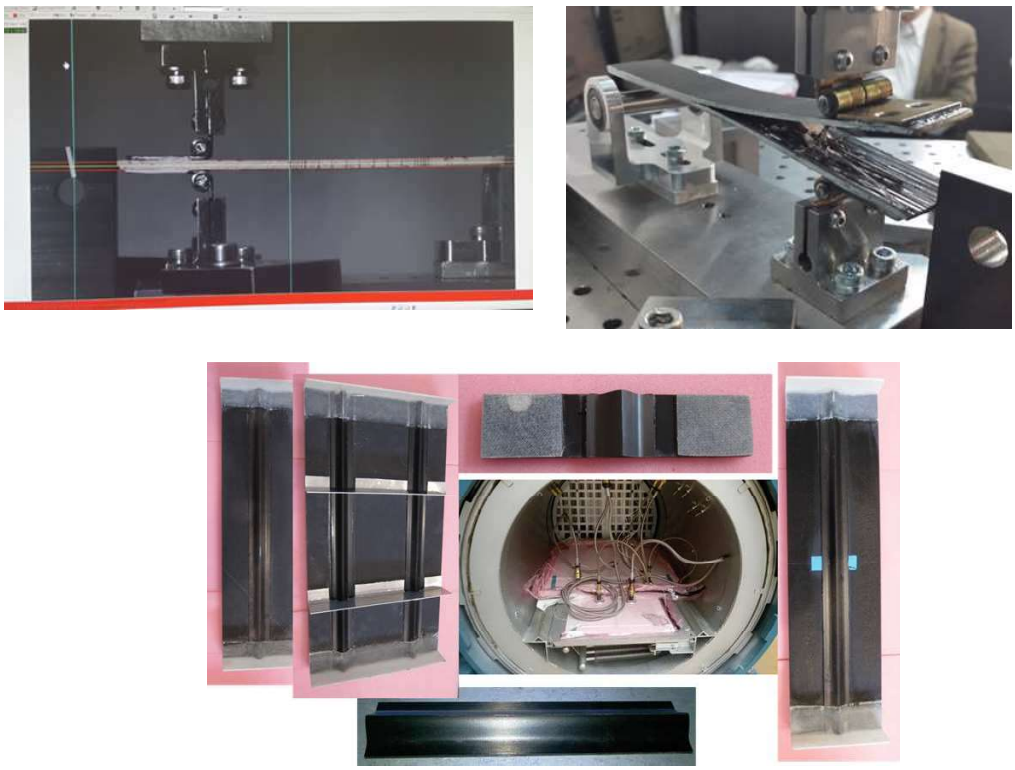

Figure 37. Test pyramid coupons used for model calibration and validation

Structural load modelling – CFD analysis

To establish realistic operation conditions for the modelled components, realistic loads acting on the structure needed to be determined. Based on data gathered during test flights (in which strain gauge signals in the chosen areas of the vertical stabilizer were collected). Aerodynamic loads constitute the main loads acting on the stabilizer. The aerodynamic analysis results suggest that the Venturi effect has a significant influence on the structural loads – in essence, the pair of stabilizers act as a constriction of the longitudinal air flow. The magnitude of this effect is related to the aircraft speed and angle of attack.

Main aim of the CFD analyses is to determine the pressure distribution on the stabilizer Surface, for various flight regimes. A particular flight regime can be described by a specific vector of flight parameter values. In addition, the pressure distribution is affected by the wing mechanization configuration. The mechanization configuration differs between the flight regimes and depends mainly on the current angle of attack – for angles of attack $\alpha > 9°$ the rear wing flaps are extended, and for landing regimes the additionally the front wing flaps are extended. In the end, the following CFD model configurations were considered:

- Model 1: extended rear and front wing flaps;
- Model 2: front wing flaps extended;
- Model 3: default wing and stabilizer configuration (surfaces in neutral position);
- Model 4: supersonic configuration;
- Model 5: front wing flaps extended, rudder deflected;
- Model 6: neutral wing configuration, rudder deflected;

- Model 7: supersonic configuration, rudder deflected.

The flight regimes and corresponding CFD configurations were chosen so as to represent the largest scope of flight conditions occurring in service. As a result, 22 flight regimes were specified (including variation in flight parameters and geometric configuration). The CFD analyses focused on determining the pressure/load distributions in certain areas of interest (i.e. mainly the vertical and horizontal stabilizers) however a simulation for the full aircraft geometry was required.

The complete analysis process resulted in a detailed pressure distribution for each of the flight regimes. Based on usage analysis these results will serve as a basis of load spectrum determination for full scale fatigue tests of the vertical stabilizer, as well as an input load for the finite element simulation of structural behaviour of damaged and repaired components.

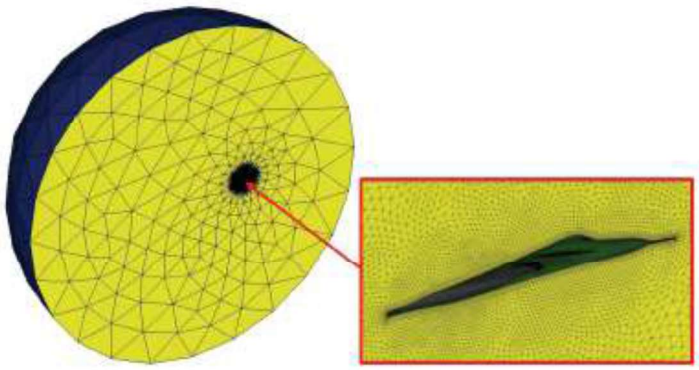

Figure 38. CFD mesh

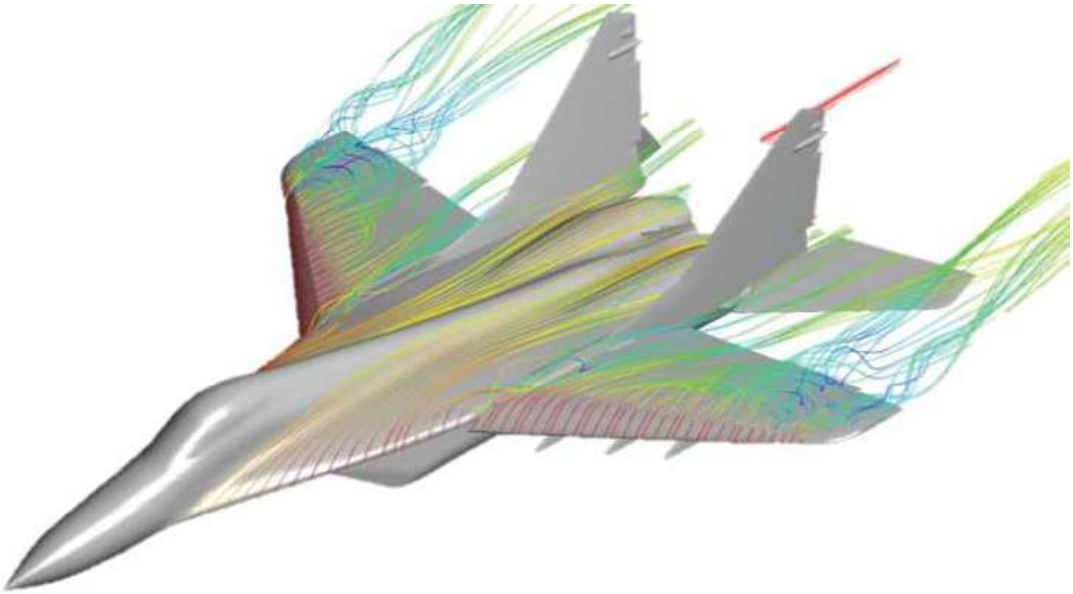

Figure 39. Example of CFD results – streamlines